Cement and Concrete Composites 145 (2024) 105338

Contents lists available at ScienceDirect

Cement and Concrete Composites

journal homepage: www.elsevier.com/locate/cemconcomp

A comprehensive micro-nano investigative approach to study the development of aluminosilicate gel in binary blends of lithium slag geopolymer

Usman Javed **, Faiz Uddin Ahmed Shaikh *, Prabir Kumar Sarker

Department of Civil Engineering, School of Civil and Mechanical Engineering, Curtin University, Perth, Australia

ARTICLE INFO

Keywords:
Lithium slag geopolymer
Micromorphological
Micromechanical
Aluminosilicate gel
Microstructural development
Carbonation

ABSTRACT

This study extensively investigates the formation of aluminosilicate gel in binary blends of lithium slag geopolymer (LSG) containing fly ash and silica fume. A comprehensive analysis of the aluminosilicate gel was performed at the micro-nano scale, employing techniques such as mineralogical, crystallographic, micromorphological, and micromechanical analysis. C-(N)-A-S-H and N-(C)-A-S-H gels were found between Si/Al ratios of 2.41–3.04 and 3.88 to 4.33, respectively. Fly ash incorporated LSG at 45% alkaline activator yielded the highest average nano-indented modulus of 22.54 GPa. Statistical Gaussian deconvolution was employed to categorize mineral phases in nano-indentation of LSG, revealing substantial distinctions indicated by the low p-values. Carbonation in silica fume incorporated LSG was affirmed by selected area electron diffraction (SAED) patterns of calcite crystallites. The microstructure of LSG containing fly ash was stiffened by the growth of needle crystals of hydroxy-sodalite and aluminosilicate gel. Thus, the formation of C-(N)-A-S-H gel and hydroxy-sodalite governs the strength development of LSG binary blends.

1. Introduction

Geopolymer is an inorganic and amorphous polymer that forms by the polycondensation of aluminosilicate precursors while reacting with alkaline activators to produce a three-dimensional Si-O-Al network structure [1–3]. It exhibits cementing properties and has a similar theoretical bond strength to aluminosilicate gel (over 12 GPa) [4], similar to that of calcium silicate hydrate in cement hydrates [5]. The development of geopolymer also offers environmental benefits by reducing carbon emissions released during clinker production [6–8]. Therefore, it is a suitable precursor for geopolymer synthesis due to the presence of high silica and alumina concentration in it.

1.1. Alkali activation of low calcium precursors

The development of microstructure in low calcium geopolymer paste matrix is due to the formation of aluminosilicate gel and zeolites. Alkali activation of fly ash was conceptualized as a reaction similar to zeolite synthesis and a model was proposed by Palomo et al. [9]. The model predicts that the reaction proceeds via two stages: (a) nucleation, and (b) growth. The first two steps proposed by Glukhovsky [10] are nucleation, which involves the dissolution of aluminates from the precursor, and geopolymerisation, which involves the synthesis of complex ionic species and is reliant on thermodynamic and kinetic parameters. The term "growth" is used to describe the gradual expansion of a crystal after its nuclei have reached a crucial size. An aluminosilicate gel known as N-A-S-H gel or 'zeolite precursor' is the primary component of the amorphous matrix with cementitious properties that result from the alkaline activation of fly ash. This gel has the potential to age and crystallize into a zeolite [11].

Multiple authors have since updated this model [12,13]. The new model proposes a sequence of steps that together constitute N-A-S-H gel formation. When the aluminosilicate material is exposed to the alkaline solution, it breaks down into several species, primarily silica and alumina monomers. In turn, these dimers react with additional monomers to form trimers, tetramers, and so on. The aluminosilicate solution achieves the saturation point, and then a metastable intermediate species, N-A-S-H gel precipitates which is rich in alumina [14]. High concentrations of Al^{3+} ions in the alkaline medium during the first minutes to hours of the reaction explain its formation; reactive aluminum dissolves more quickly than silicon because Al-O bonds are weaker than

* Corresponding author.
** Corresponding author.
E-mail addresses: usman.javed@curtin.edu.au (U. Javed), s.ahmed@curtin.edu.au (F.U.A. Shaikh).

https://doi.org/10.1016/j.cemconcomp.2023.105338
Received 3 May 2023; Received in revised form 14 September 2023; Accepted 14 October 2023
Available online 16 October 2023

Abbreviations

LSG	Lithium Slag Geopolymer
C-(N)-A-S-H Gel	Calcium-Sodium Aluminosilicate Hydrate Gel
Si-O-Al	Silicon-Oxygen-Aluminium
GPa	Giga-Pascal
N-A-S-H	Sodium Aluminosilicate Gel
N-(C)-A-S-H Gel	Sodium-Calcium Aluminosilicate Hydrate Gel
STEM	Scanning Transmission Electron Microscopy
SAED	Selected Area Electron Diffraction
Na_2O	Sodium Oxide
SiO_2	Silicon-di Oxide
$Na_2B_4O_7.10H_2O$	Sodium Tetraborate Decahydrate
SEM	Scanning Electron Microscopy
EDS	Energy Dispersive Spectroscopy
TIMA	TESCAN Integrated Mineral Analysis
XRF	X-Fluorescence
BF-image	Bright Field
HAADF	High-Angle Angular Dark Field
STEM	Scanning Transmission Electron Microscopy
CCD	Charge Coupled Device
BSE	Backscattered Electron Micrograph
SE	Secondary Electron Micrograph
Si/Al	Silica to Alumina Ratio
Ca/Si	Calcium to Silica Ratio
PDF	Probability Density Function
ITZ	Interfacial Transition Zone
ANOVA	Analysis of Variance
HRTEM	High-Resolution Transmission Electron Microscopy

Si-O bonds. Upon further dissolution of Si-O species, the raised silicon concentration undergoes structural changes to form a stable gel (N-A-S-H). Many of the physical properties are established by the polymer's final composition and the pore microstructure and distribution, both of which are determined by structural reorganization.

1.2. Geochemistry and micro-mechanics of gel matrix

Inorganic polymers such as geopolymers are synthesized by reacting alkali activators with aluminosilicate-rich precursors to form a three-dimensional network of Si-O-Al bonds. The strength of geopolymer is governed by the structural properties of long-chained Si-O-Al bonds in N-(C)-A-S-H gel. It is a fact that increased activator content marked by the higher concentration of monovalent cations i.e. (Na+) and (K+) stabilizes the negatively charged AlO^4 tetrahedron and forms a long chain network structure of polysialate [15]. Various studies have characterized the gel matrix of geopolymer develop using various precursors. Mills et al. [1] investigated the nano-scale microstructure of aluminosilicate gels with varying concentrations of aluminum and results indicated that the 15-20 nm gel matrix became more spherically defined upon the addition of aluminum, whereas Chen and Mondal [16] reported the increased the size, thus resulting N-A-S-H gel smoother and round upon addition of NaOH in geopolymer paste matrix. Zhu et al. [17] investigated the alkali-activated incinerated bottom ash that the presence of aluminosilicate gel along with the presence of C-S-H gel, and the nano structural connectivity of aluminosilicate-gel was similar to that of alkali-activated fly ash along with Si/Al ratio of 2.52.

The quality of N-(C)-A-S-H solely depends on the chemical, morphological, and crystallographic attributes of precursor material, while keeping other variables constant (variables such as temperature, activator content, curing conditions, and time). Chemically similar to fly ash, lithium slag is a source of aluminosilicate with a lower calcium content. The aluminosilicates are present in the form of spodumene, anorthite, albite, amorphous phase, and some traces of other types of plagioclase feldspars [18–20]. The aluminosilicate in the form of an amorphous phase is more reactive than the minerals with well-defined crystal structures and orientations [21]. The percentage of amorphous aluminosilicate in lithium slag varies depending upon the processing, the maximum value of amorphous phase was identified by calcining lithium slag at 700°C at a temperature ramp of 3°C/minute [22]. Owing to the presence of higher aluminosilicates lithium slag contains the desired geochemistry, however, higher percentages of sulfur in the form of anhydrite/gypsum are potentially undesirable for the formation of zeolites and aluminosilicate gel. The higher sulfur content originates upon the leaching of the spodumene ore for the extraction of lithium during refining processing [20,22]. Higher concentrations of sulfate appear to induce cracking in aluminosilicate gel as reported by the published literature [18], in which the deleterious effect of sulfate is mitigated by the incorporation of sodium tetraborate, other precursors such as fly ash and silica fume. However, the effect of a higher concentration of alkaline activator could also potentially suppress the formation of sulfur species in the aluminosilicate gel, thus improving the mechanical properties of geopolymer.

The authors' previous research on LSG with fly ash and silica fume investigated its microstructural properties at a lower alkaline activator and higher water-to-precursor ratio; this new study expands on that research which aims to characterize the aluminosilicate gel matrix in fly ash and silica fume incorporated geopolymer paste matrix at higher content of alkaline activator by investigating micro-morphology, crystallography, mineralogy, and micromechanical properties. LSG containing silica fume was further investigated for carbonation reaction by Scanning Transmission Electron Microscopy (STEM), Selected Area Electron Diffraction (SAED), and Rietveld quantitative analysis for identifying and quantifying the calcite polymorphs. The micromechanical properties such as elastic modulus and hardness of LSG from nanoindentation were correlated with compressive strength, thereafter the aluminosilicate gel matrix was further mechanically classified by the gaussian deconvolution of elastic moduli obtained from nanoindentation analysis. Conclusively, this study investigated the mineralogy, micromorphology, and micromechanical characteristics of LSG under elevated levels of alkaline activator content. The aim was to elucidate the correlation among these properties at the micro and nanoscale, for understanding the strength development of LSG.

2. Materials and methods

2.1. Materials

Lithium slag, silica fume, and fly ash were used as raw materials. After calcination at 700 °C, the lithium slag was rapidly cooled by exposing it to room temperature followed by grinding in a ball mill for half an hour. This thermo-mechanical processing helps to increase the amorphous phase [18,19]. Ecotec Silica Fume supplied densified silica fume with a specific surface area of 15–30 m^2/kg. To prevent the flash set of LSG in the presence of silica fume, sodium tetraborate (borax) was used as an admixture. The chemical oxide compositions of lithium slag, silica fume, and fly ash are shown in Table 1. Alkaline activators were sodium hydroxide and sodium silicate. The molarity of the sodium hydroxide solution was 10 M, whereas the sodium silicate contained 14.70, 29.40, and 55.90% Na_2O, SiO_2, and water, respectively and powdered borax was used containing 99% concentrated sodium tetraborate decahydrate ($Na_2B_4O_7.10H_2O$)..

Table 1
XRF of raw lithium slag, fly ash, and silica fume.

Oxides	SiO_2	Al_2O_3	Fe_2O_3	CaO	MgO	MnO	TiO_2	SO_3	P_2O_5	K_2O	Na_2O	LOI
Lithium slag	54.53	21.08	1.45	7.53	0.57	0.23	0.05	5.62	0.48	0.88	0.72	6.76
Silica Fume	94.58	0.50	0.06	1.54	0.41	-	-	0.14	0.11	0.64	0.23	1.79
Fly ash	55.90	26.94	6.59	4.25	1.51	0.10	1.43	0.20	0.50	0.76	0.31	1.51

2.2. Characterization of precursors

Lithium slag was characterized by various microstructural analytical techniques such as Scanning Electron Microscopy along Energy Dispersive Spectroscopy (SEM/EDS), Tescan Integrated Mineral Analysis (TIMA), X-ray diffraction, Rietveld Quantitative analysis. The chemical composition was determined using X-ray Fluorescence (XRF), and the crystallographic and mineral phases were quantified using XRD Rietveld refinement and TIMA, respectively. Fluorite was used as an internal standard for Rietveld quantitative refinement. The rest of the sample preparation and analysis parameters of all characterization techniques were kept similar to those of the authors' previously published studies [18,19].

2.2.1. Morphology of precursors

The microstructural morphology of the lithium, sodium tetraborate decahydrate, fly ash, and densified silica fume was determined by SEM/EDS, and is presented in Fig. 1-a, b, c, respectively. The size of the fly ash particles ranged between submicron to 10 μm, whereas smaller particles appeared more indicating the presence of traces of iron on the EDS spectrum, indicating its origin from ferrous-rich minerals. Lithium slag contains calcium-rich aluminosilicates in the form of micro and nano-sized angular particles. However, the prismatic particles sized between 20 and 170 μm, are rich in sulfate in the form of calcium sulfate originating from the acid leaching and roasting of spodumene ore for lithium extraction. Sodium tetraborate decahydrate (borax) shows the EDS spectrum of sodium and oxygen, without visible boron peak as of its lower atomic number [23]. The BSE micrograph of densified silica fume

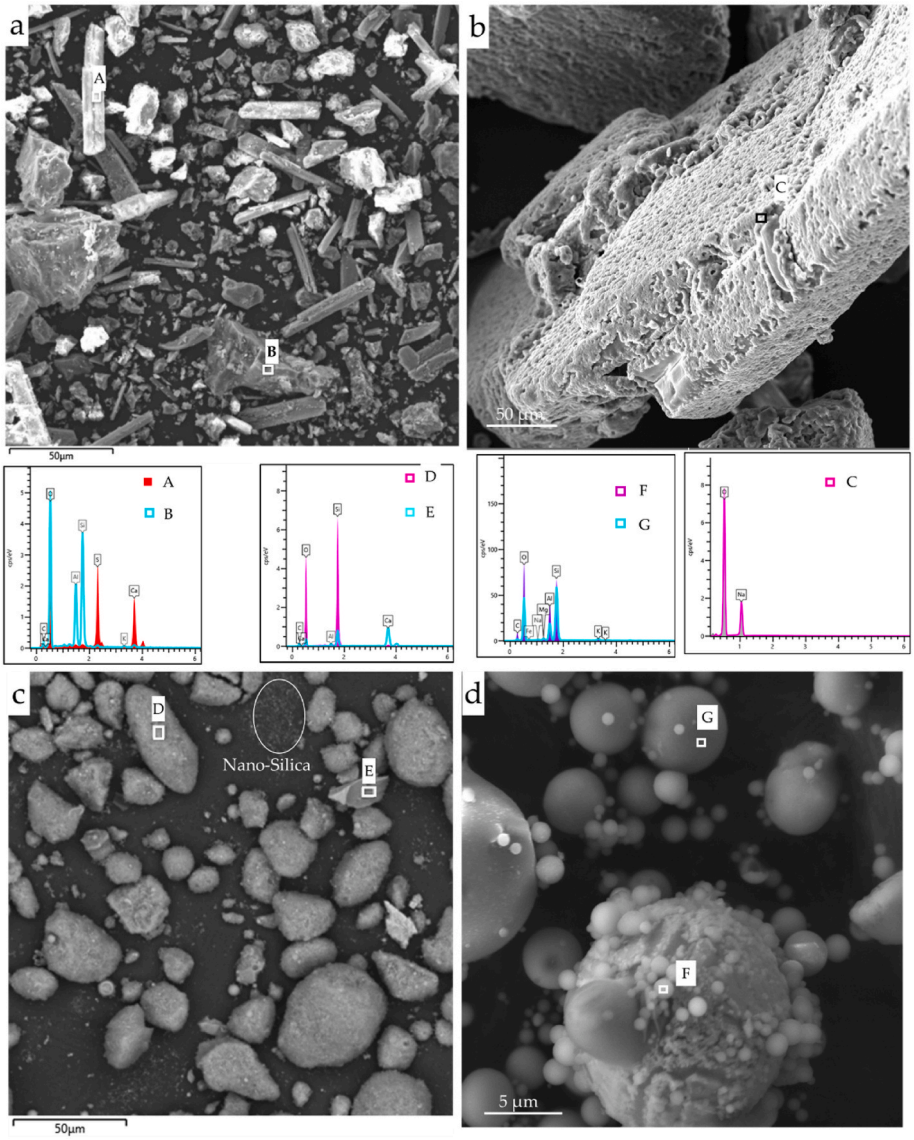

Fig. 1. Morphology of a) Raw lithium slag [18] b) Sodium tetraborate decahydrate c) Densified silica fume (BSE) d) Fly ash.

presents the round particles of silica fume along with the nano-silica phase attached to the surface of micron-sized particles which have the potential to readily react during alkali activation.

2.2.2. Mineralogy and crystallography of precursors

The mineralogy analysis of lithium slag suggests that it contains aluminosilicate in the form of spodumene, anorthite, and traces in some other members of the feldspar group such as albite as shown in Fig. 2. Its oxide composition containing cumulative oxides of silicon, aluminum, and iron is 77.06%, whereas the average particle size (D_{50}) of raw lithium slag is 42.01 μm. Laser diffraction particle size analysis of lithium slag indicated that it contains a high fraction of particles between 20 μm and 200 nm [19]. As per the chemical requirements, fly ash qualifies as class F fly ash containing a cumulative concentration of SiO_2, Al_2O_3, and Fe_2O_3 higher than 70% [24]. The Rietveld refinement of precursors is shown in Fig. 3, in which the calcined lithium slag resulted in over 80% amorphous phase along with crystalline aluminosilicate minerals of 5.35, 2.01, 0.93, 0.55% as anorthite, spodumene, albite, and muscovite, respectively, whereas silica is also contributed by 4.59% of quartz [19]. The crystalline component of aluminosilicate in fly ash was in the form of albite, mullite, and anorthite along with 7.87, 7.39, and 5.23%, respectively, whereas the rest of the amorphous aluminosilicate contributed toward amorphous phase content of 65.16%. However, crystalline silica in the form of quartz and cristobalite was detected and quantified in silica fume as 26.20, and 16.71% respectively, and the amorphous silica was 57.07%.

2.3. Mix proportion

LSG mixes containing additive incorporation of fly ash and silica fume as supplementary precursors were formulated based on the suggestions of the author's previously published research which are shown in Table 2a, b [18]. However, the molarity of sodium hydroxide was selected as 10 M and the mixes were tested at alkaline activator content of 45 and 55% for fly ash incorporated geopolymer, whereas silica fume replaced geopolymer mixes were cast at 45% only. The ratio between sodium silicate and sodium hydroxide was kept constant at 3. For silica fume incorporated LSG, alkaline activator content and percentage silica fume incorporation were selected after the iteration of trial mixes. Also,

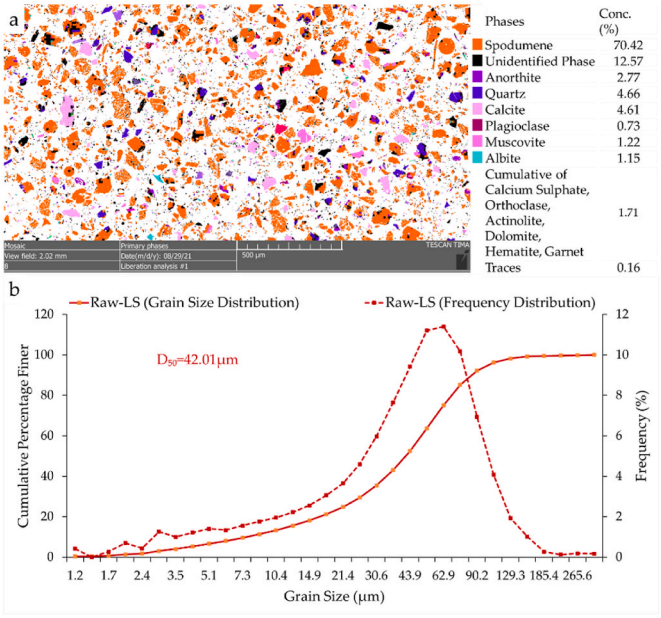

Fig. 2. Particle characterization of raw lithium slag a) Mineralogy and b) Particle size distribution of raw lithium slag by automated mineral analysis [18].

the net silica to alumina ratio in silica fume incorporated geopolymer was varied as 3.04, 4.25, and 6.28 at 0, 20, and 40% of silica fume incorporated geopolymer mixes as shown in Table 2b. Additionally, 3% sodium tetraborate decahydrate was added in all mixes to retard the flash setting of geopolymer for better strength development [20,22].

2.4. Geopolymer synthesis and curing

Geopolymer specimens containing fly ash and silica fume were prepared by dry mixing the corresponding constituents in a Hobart mixer for the 30s at 116 revolutions per minute (rpm), followed by pouring the mixture of alkaline activators in dry mix and mixed for 2 min at the speed of 380 rpm. The fly ash geopolymer paste was poured into 50×50×50 mm^3 cube moulds and cured in an oven at 70 °C for 24 h after wrapping with a polyethylene sheet to avoid moisture loss and microcracking. After 24 h of heat curing, fly ash LSG paste specimens were kept at 25 ± 1°C and 90% relative humidity till the testing age. Whereas silica fume incorporated mixes after wrapping in polyethylene sheet were kept at 25° ± 1°C till the age of testing and heat curing was avoided to mitigate strength degradation as evident in the literature [18]. After curing at testing age, the mortar cube specimens (50×50×50 mm^3) were tested for compression.

2.5. Testing program

For micro and nanoscale characterization of the aluminosilicate gel matrix, specimens after curing for 28 days were cut into 5×15×15 mm sized chips using a speed-adjustable cutter at 270 rpm. The specimens were stored in acetone for 48h to stop the geopolymerization and remove pore water without damaging the nanostructure [25,26], thereafter, specimens were stored in a vacuum desiccator to avoid carbonation.

2.5.1. Microstructure, mineralogy, and crystallographic of LSG gel matrix

2.5.1.1. Microstructural analysis. The microstructural analysis of LSG containing partial replacement of fly ash and silica fume under high-resolution Field Emission Scanning Electron Microscopy (FESEM) TESCAN MIRA3 equipped with an in-beam secondary electron, backscattered electron, and EDS detectors controlled by Aztec software, Oxford instruments. The SEM-EDS was conducted on carbon-coated geopolymer specimens of size 5×15×15 mm for characterizing micromorphology, and composition of LSG aluminosilicate gel matrix at a working distance of 14 mm and beam intensity of 14 kV both imaging and EDS. Whereas, the vacuum-desiccated geopolymer specimens were coated with a 20 nm layer of carbon coating.

2.5.1.2. Mineral composition. The mineral composition of the aluminosilicate gel matrix was identified and quantified by automated SEM-EDS using TESCAN Integrated Mineral Analyzer (TIMA) which is also high-resolution field emission (FESEM) coupled with four EDS detectors for fully automated and high-speed EDS spectra acquisition speed. The TIMA analysis was conducted on vacuum-impregnated resin geopolymer specimens ground up to a roughness of 1 μm, which were prepared as per protocols followed in the authors' previous study [19]. A represented 8 × 8 mm^2 area was selected for analysis, which produced backscattered micrographs, phase maps, and mapped EDS spectral maps along with offline operable capabilities. The analysis parameters including electron beam energy, probe current, and beam intensity were 25 keV, 5.33 nA, and 18.80, respectively. The high-resolution dot scanning mode, spot size, working distance, and pixel size were 79.66 nm, 15 mm, and 1 μm, respectively. After TIMA analysis, EDS spectra were post-processed to identify and quantify the unknown phase using the TESCAN TIMA software v2.5.2 mineral library.

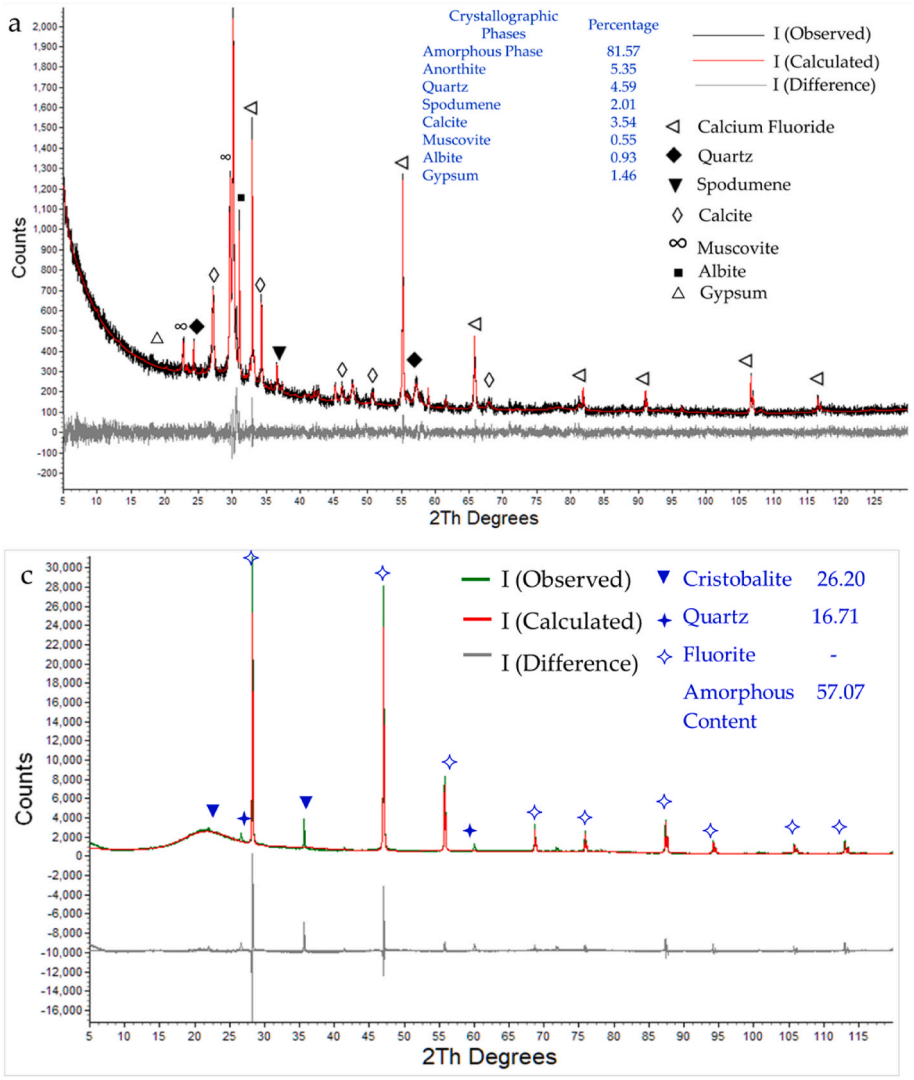

Fig. 3. Rietveld quantitative analysis of a) Calcined lithium slag [18] b) Fly ash c) Silica fume.

Table 2a
Mix proportions of LSG containing fly ash as the supplementary precursor.

Activator (%)	Geopolymer Mixes	Lithium Slag (kg/m^3)	Fly ash (kg/m^3)	Sodium Hydroxide (kg/m^3)	Sodium Silicate (kg/m^3)	Borax (3%)
45	$100LS0FA_{45}$	1415.87	0	159.28	477.85	42.47
	$50LS50FA_{45}$	707.93	707.93	159.28	477.85	42.47
	$0LS100FA_{45}$	0	1415.87	159.28	477.85	42.47
55	$100LS0FA_{55}$	1415.87	0	194.68	584.04	42.47
	$50LS50FA_{55}$	707.93	707.93	194.68	584.04	42.47
	$0LS100FA_{55}$	0	1415.87	194.68	584.04	42.47

Note: $Na_2SiO_3/NaOH = 3$, Molarity of NaOH = 10 M.

Table 2b
Mix proportions of LSG containing silica fume as a supplementary precursor.

Activator (%)	Geopolymer Mixes	Lithium Slag (kg/m^3)	Silica Fume (kg/m^3)	Sodium Hydroxide (kg/m^3)	Sodium Silicate (kg/m^3)	Borax (3%)	SiO_2/Al_2O_3
45	$100LS0SF_{45}$	1415.87	0.00	159.28	477.85	42.47	3.04
	$80LS20SF_{45}$	1132.69	283.17	159.28	477.85	42.47	4.25
	$60LS40SF_{45}$	849.52	566.34	159.28	477.85	42.47	6.28

Note: $Na_2SiO_3/NaOH = 3$, Molarity of NaOH = 10 M.

2.5.1.3. Crystallographic properties. Quantitative X-ray diffraction (XRD) and Rietveld quantitative analysis identify and quantify LSG paste crystal phases. Bruker D8 Advance Diffractometer Cu_Kα (1.504 Å) X-ray emission source was used for diffraction at 40 mA and 35 kV. The primary, and secondary soller radius, angular range, FDS angle, and soller axial convolution was 280 mm, 4°, 1°, and 2.5°, respectively and the rest

of the parameters were kept similar as reported in the literature [19]. DIFFRAC EVA software was used with International Crystallographic Diffraction Data (ICDD, PDF-2 release 2019) for identifying the crystallographic peaks. The rectangular chunks of LSG geopolymer stored in a vacuum desiccator were ground in a ring mill and then micronized in ethanol for 10 min with a 10% calcium fluoride control. The micronized LSG sample was dried on a hotplate at 40 °C for 24 h, and the residual powdered sample was gradually filled in an acrylic sample holder with a glass slide to avoid crystal orientation [27].

2.5.2. Micromechanical properties of aluminosilicate gel

Nanoindentation, widely recognized as a reliable technique for determining the local elastic modulus and hardness [28,29], was used to analyze the micromechanical properties of LSG paste. The nanoindentation test equipment (Agilent G200) with a Berkovich indenter tip was employed in this investigation because of load resolution down to 50 nN and displacements to 0.01 nm. The maximum indentation load was 490 mN equivalent to 50 gf (gram-force) of electromagnetic force on the indenter head [30]. The indentation was started with the constant rate of 8.88 mN/s until the maximum load of 480 mN was achieved. The average indentation depth of around 5 μm was detected, whereas the specimens were ground and polished to 1 μm, minimizing the effect of roughness on the indentation results.

The grid nanoindentation mode was selected for measuring the hardness and elastic modulus of unreacted lithium slag particles, fly ash, and silica fume particles. For each sample, a 200x200 grid was selected with the indentation points parted by 20 μm. The gap between indentation points was 4 times larger than the average indentation depth to minimize the effect of interaction which should normally remain between 3 and 5 [31]. A typical indentation grid of 200 × 200 μm is shown in Fig. 4.

The obtained load-displacement curves were utilized to calculate the elastic modulus (E) and hardness (H), which can be derived from load-displacement curves [32,33], using the following Eq. (1):

$$E = \left(1 - \nu^2\right) \cdot \left[\frac{1}{E_r} - \frac{\left(1 - \nu_i^2\right)}{E_i}\right]^{-1} \quad (1)$$

Where E and v represent the specimen's elastic modulus and Poisson ratio, E_i and ν_i represent the indenter's tip modulus and Poisson ratio, respectively. The value of v for alkali-activated materials ranges between 0.13 and 0.26 [34,35], it won't contribute significant error as per eq (1), however, the value of v was kept at 0.18.

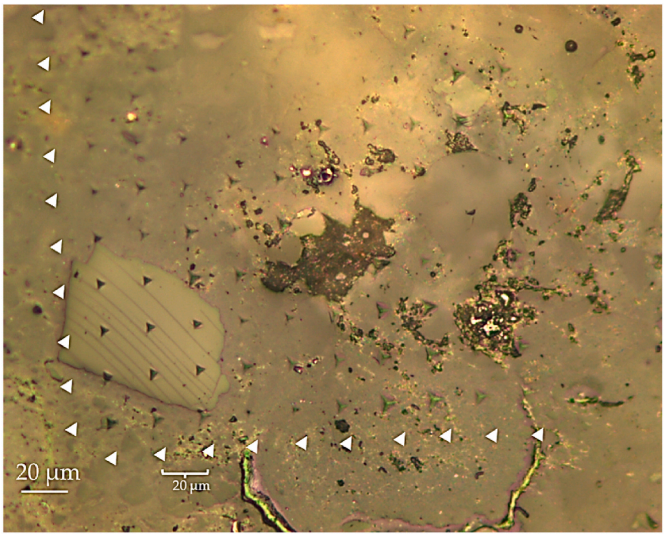

Fig. 4. Typical light microscope micrograph of 200 × 200μm grid containing impressions of Berkovich indenter on LSG containing 40% silica fume.

2.5.3. Nano-structural characterization of aluminosilicate gel

For characterizing aluminosilicate gel, a geopolymer specimen with higher hardness and elastic modulus values was selected to conduct STEM and SAED. LSG paste containing 40% silica fume was removed from the vacuum desiccator and grounded by mortar and pestle. The finer residue was selected to make a suspension in ethanol to maximize the chances of capturing the aluminosilicate gel and avoiding unreacted mineral particles. The suspension of ethanol was made with the proportion of 1 mg of powder to 5 ml of ethanol which was subsequently treated ultrasonically for unclogged particles, thereafter, a drop of sample suspension was carefully deposited on a carbon-coated copper grid which was resting on a piece of filter paper. The excessing amount of ethanol was removed through the capillary action of filter paper and repeated the process for a second drop of suspension. The copper grid was dried overnight, thereafter, STEM, SAED, and EDS analyses were carried on.

A transmission electron microscope (FEI Talos F200X, ThermoFisher Scientific) equipped with a 200 kV Field Emission Gun (FEG), and four in-column SSD super-X EDS detectors was used for STEM, EDS, and SAED analysis, operating with an accelerating voltage of 200 kV.

For the characterization of aluminosilicate gel, a highly focussed electron beam scanned over the specimen, whereas the specimen was analyzed by generating bright field and dark field images by using a Bright Field (BF) detector and High-Angle Angular Dark Field (HAADF) detector featuring the submicron morphology, and composition. However, the small region of interest containing aluminosilicate gel was bombarded with a highly focussed beam of electron, and the scattered electron generated a diffraction pattern collected on Charge Coupled Device (CCD). For elemental analysis of aluminosilicate gel, EDS elemental spectra were mapped on STEM-BF and STEM-HAADF images.

3. Results and discussion

3.1. Micromorphology of gel matrix

The microstructural morphology of LSG, fly ash incorporated LSG and silica fume-added LSG mixes are presented in Fig. 5a and b, c-d, and e-f, respectively. The micrographs contain both secondary electron (SE) micrographs and backscattered electron (BSE) micrographs revealing the products of alkali activation.

In LSG at 45% alkaline activator, SEM micrograph (Fig. 5b) revealed aluminosilicate gel matrix with bright, dense, and featureless microstructure. Compared to the authors' previous study at 35% alkaline activator, the extent of both geopolymerization and microstructural development are higher at 45% alkali activator content [18]. EDS analysis (EDS A) showed that increasing the alkaline activator from 35 to 45% increased N-(C)-A-S-H gel development despite LSG cracking in the weak zone. 50% of fly ash replacement in LSG was attributed to aluminosilicates in the gel matrix and caused the pore refinement by surface reactivity of micro-nano-sized fly ash cenospheres for better gelling in the microstructure. The BSE micrograph (Fig. 5d) illustrates that the geopolymerization renders cenospheres below 5 μm more brighter in BSE micrograph which is indicative of the geopolymer products with higher atomic numbers possibly the cenospheres are encapsulated with long-chained aluminosilicate gel. The alkaline activator etches the outer surface of cenospheres, penetrates, and reacts with hollow fly ash particles, increasing their surface area (Fig. 5d). The higher exposed area offered more susceptibility to geopolymerization, thus, improving microstructure by increasing the surface area exposed for aluminosilicate dissolution. Fig. 5d reveals that the smaller fly ash particles undergo more aluminosilicate dissolution than bigger cenospheres. At EDS B, the fly ash cenosphere reacted over 40% of the alkaline activator, exposing the inner morphology with small holes and cracks. Some ruptured cenospheres were visible in dark regions in the same BSE micrograph. An angular microstructure shows the reaction products of lithium slag particles by partial dissolution of

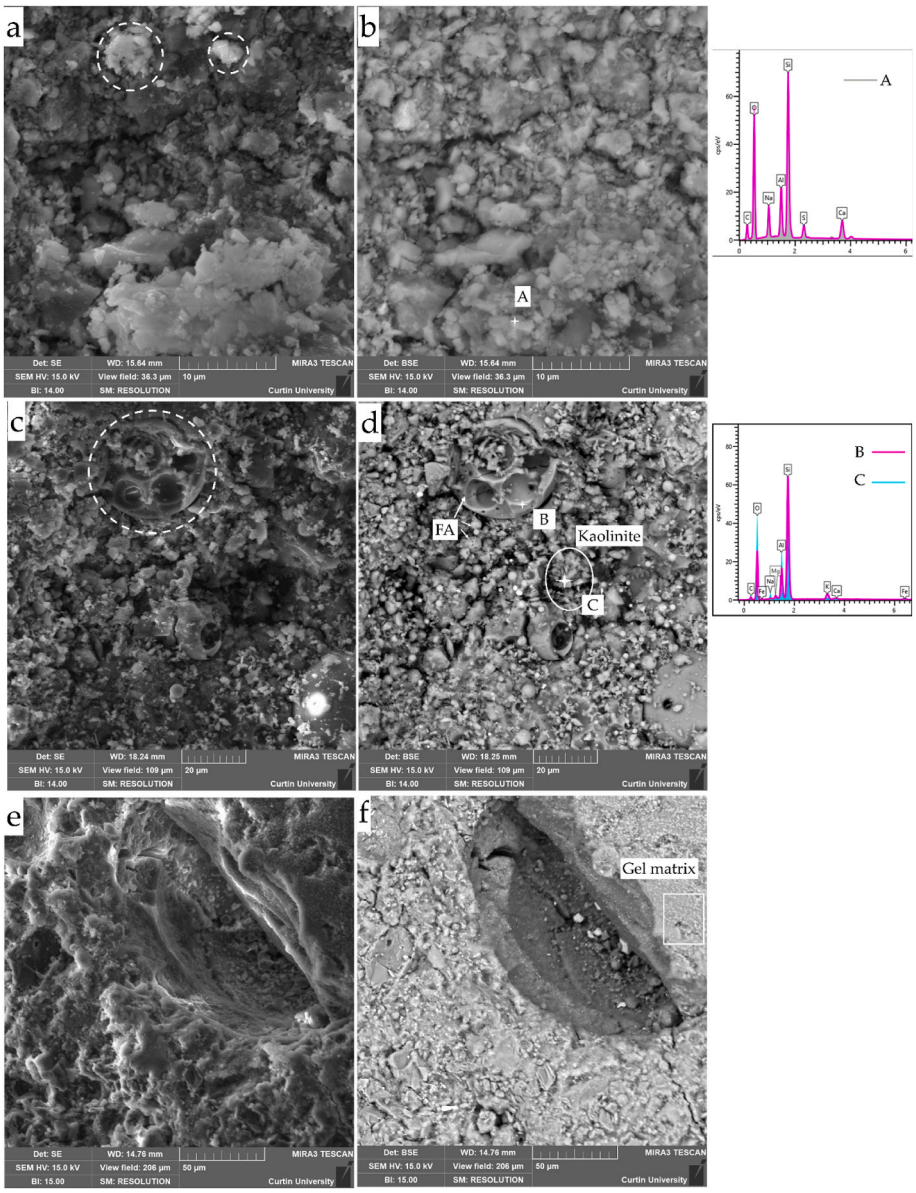

Fig. 5. The micromorphology and EDS of a, b) 100LS0FA$_{45}$; c, d)50LS50FA$_{45}$ e, f) 60LS40SF$_{45}$

aluminosilicate, while a flaky plate-like microstructure with partially geopolymerized particles represents kaolinite particles as per EDS spectrum C and high-magnification micrograph (Fig. 5d).

The micrograph with 40% silica fume shows a denser aluminosilicate gel with the fewest pores and voids. Due to the higher silica content, it is difficult to identify individual particles except for the BSE micrograph (Fig. 5e and f), indicating a higher degree of aluminosilicate dissolution. The minute particular growth contains traces of iron and magnesium

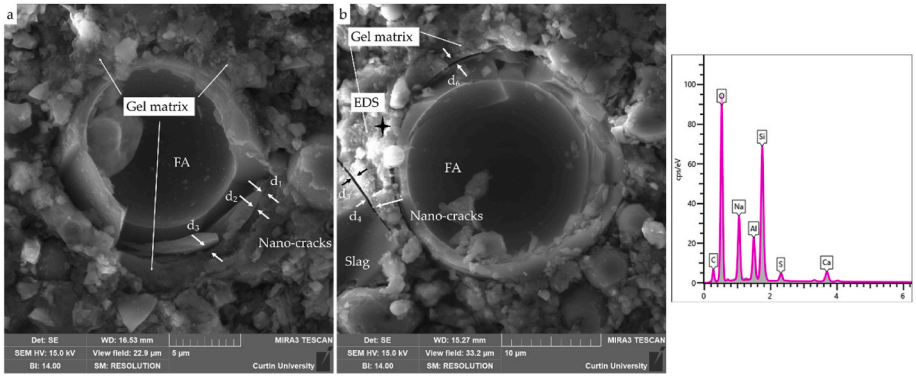

Fig. 6. Interfacial crack width of 50LS50FA at (a) 45, and (b) 55% of alkaline activator.

alongside alkali (Na, Ca) aluminosilicates marked by a brighter microstructure in the BSE micrograph.

The Si/Al ratio was highest in silica fume incorporated LSG with the value of 5.2 and ranged between 2.6 and 3.5 for gel near fly ash cenosphere, whereas the lowest was recorded for kaolinite particle (2.15). As per the literature [36,37], better microstructural properties are achieved at Si/Al between 2.5 and 3. Therefore, from the Si/Al ratios, better dissolution of aluminosilicate occurred in LSG containing fly ash, whereas silica fume mix revealed too high silica concentration.

The crack-width at the interface of fly ash particle and aluminosilicate gel of LSG containing fly ash is shown in Fig. 6 and Table 3. High-resolution SEM micrographs depicted the partially broken fly ash particle engrossed in an aluminosilicate gel matrix of LSG containing fly ash at 45 and 55%, respectively. The surrounding microstructure of the broken fly ash cenosphere represents the aluminosilicate gel as shown in the EDS spectrum. The microstructure of fly ash incorporated gel matrix at 55% activator content resulted in to densified gel matrix around the particle as of the higher dissolution of aluminosilicates by increased alkalis ions (Na+) in the geopolymer paste matrix. However, the average crack width of the geopolymer mix at 45% of alkaline activator was 76.14 μm, which is three times lower than the mix containing 55% alkaline activator (219.80 μm). Although the densification of the gel matrix occurred at a higher concentration of alkaline activator, the wider average crack width indicates the possibility of thermal cracking attributed to the cumulative effect of heat curing and heat evolved during geopolymerization [38,39]. Therefore, wider crack width at 55% alkaline activator could contribute toward the degradation of mechanical properties. Hence, LSG mix containing fly ash could optimally develop mechanical properties up to 45% of alkaline activator, and beyond that percentage, the drop could be observed in strength properties.

The microstructure of $50LS50FA_{45}$ and $50LS50FA_{55}$ is presented in Fig. 7a and b, c-d, respectively. N-(C)-A-S-H gel's microstructure has not evolved at 45% alkaline activator, but at 55% activator, it is dense and has granular outgrowth. The outgrowth contains sodium, silicon, aluminum, calcium, and sulfur impurities and may be poorly crystalline sodium zeolite formed by alkaline activation with sodium silicate and aluminate species. Similarly, Rios et al. [40] synthesize Na-X and Na-A zeolites from kaolin and obsidian by alkaline fusion in hydrothermal conditions. Na-X zeolites from obsidian, an aluminosilicate source material, have the micro-morphology shown in Fig. 7c.

The bright nano-sized needle microstructure shows hydroxy-sodalite at 45% and 55% alkaline activator in Fig. 7b and d, respectively. The LSG containing fly ash with 55% activator content developed more matured hydroxy-sodalite. In the mix with 55% alkaline activator, hydroxy-sodalite crystals are 100–200 nm thick and 400-500 nm long, while in the mix with 45% activator, the crystals are 80–100 nm thick and 450-500 nm long. Hydrothermal conditions at 70°C yield hydroxy-sodalite from sodium hydroxide and sodium silicate reacting with fly ash aluminosilicate. Its formation is more pronounced at 55% of the activator, whereas at 35% alkaline activator, no adequately developed crystals are formed which could be detected in SEM analysis. In perspective to the mechanical properties of LSG containing fly ash, hydroxy sodalite reinforce the skeleton of aluminosilicate gel, its presence in microstructure offers fire resistance owing to its mesoporous nature that initiates vapor transport properties as evident from the literature [41,42]. Klima et al. [41] incorporated sodalite in fly ash geopolymer after synthesizing it consulting a published study [43]. The results suggested that 5% incorporation of synthesized sodalite in fly ash geopolymer enhances thermal resistance up to 800°C attributed to its mesoporous nature, reducing the chances of spalling in during the heating cycle. Similarly, Chen et al. [42] investigated the effect of the generation of hydroxy sodalite on the compressive strength of fly ash geopolymer and reported 110.2 MPa compressive strength after 28 days of curing at hydrothermal conditions (75°C) for 24h. Conclusively, LSG at 45% of alkaline activator performs well in terms of lower crack width that might have undergone optimum geopolymerization. However, the incorporation of silica fume enhanced the Si/Al ratio and reduced the porosity in LSG paste matrix.

3.2. Quantitative minerology of aluminosilicate gel

The automated mineral analysis of LSG, which contains 35, 45, and 55% of alkaline activators, is shown in Fig. 8. LSG mix with 35% of the alkaline activator is included in the literature, for comparison in strength development. The main aluminosilicate minerals in lithium slag were spodumene, albite, and anorthite, with weight percentages of 60.08, 6.48, and 1.21%, respectively. The concentrations of albite, mordenite, and anorthite were 45.96, 28.62, and 14.40 in LSG containing 35% of the activator; 34.09, 31.61, 23.69% at 45% of the activator; and 35.85, 27.05, 26.87% at 55% of the alkaline activator, respectively. However, after geopolymerizing lithium slag at 35% activator, the least dissolution of aluminosilicate was observed for spodumene, which transformed to albite after the ion exchange of Li^+ with reacting Na^+ ions along with a slight change in aluminosilicates as a result of alkali activation as reported in the literature [19]. It can be deduced from the results that the dissolution of aluminosilicate from micro-sized spodumene particles has not extensively occurred, it might just chemically reacted with the alkaline activator and sodium ions chemically ingresses, thereafter reacted with particles, as; a) Si/Al ratio of albite remained between 1.84 and 2.23 b) only traces of Na detected in EDS spectrum c) the particle morphology remains unchanged even after geopolymerization. Whereas, the dissolution of aluminosilicate occurred from anorthite, albite, and plagioclase to form aluminosilicate gel like anorthite and mordenite as the Si/Al ratio of stated minerals reached closer to 3 and this aluminosilicate gel encapsulates the particles. According to the TIMA analysis, calcium-bearing minerals such as $CaSO_4$, calcite, and amorphous phase containing calcium reacted with the aluminosilicate at higher alkalinities to form aluminosilicate gel that filled the voids with a chemical composition matching with anorthite. Additionally, the sodium-based activator reacted with aluminosilicate particles at higher alkalinity to form a porous aluminosilicate product chemically like mordenite, which is also contributing to filling micro voids among lithium slag particles in the LSG paste matrix. Mordenite is present in LSG at a lower concentration than in LSG with fly ash addition. This gel fills in all the voids and gaps, and as the alkaline activator concentration increased, more anorthite was produced in the precursor particles. Anorthite is formed when aluminosilicates are combined with calcium from calcium-bearing minerals like calcium sulfate and calcium carbonate to fill the voids between the tiny particles.

According to automated SEM/EDS results (Fig. 8), the aluminosilicate gel in LSG containing 50% of fly ash is identified as anorthite and mordenite. This gel is a long-chained amorphous tetrahedron of alumina and silica attached to the species of alkalis (Na, Ca). The concentrations of anorthite, mordenite, and albite in LSG that included fly ash were 53.17, 28.88, and 8.69% when using a 35% alkaline activator, and 49.18, 29.32, 13.24% when using a 45% alkaline activator. At 35% of alkaline activator in LSG with fly ash, the concentration of mordenite

Table 3
Interfacial crack widths on the juncture of fly ash cenospheres and aluminosilicate gel.

Crack width (nm)	d_1	d_2	d_3	d_4	d_5	d_6	Average crack width (nm)
$50LS50FA_{45}$	49.61	87.58	91.24				76.14
$50LS50FA_{55}$				232.59	261.14	165.68	219.80

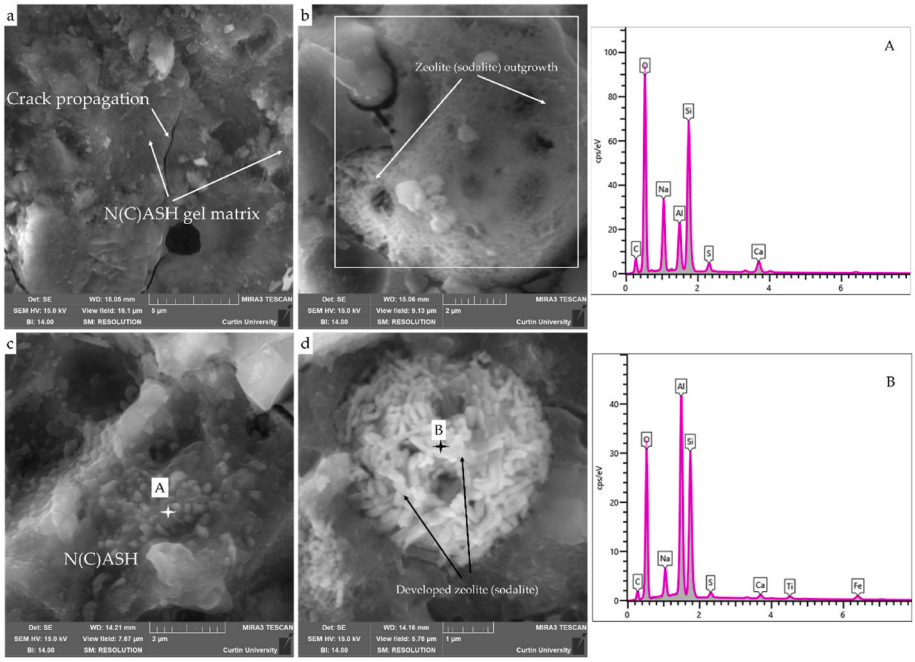

Fig. 7. Microstructure development of LSG containing fly ash at 45% (a, b) and 55% (c, d) of alkaline activator.

was as high as 53.17%, but after adding 45% of alkaline activator, the concentration of mordenite dropped to 29.32% and the concentration of anorthite rose to 49.18%. The Si/Al ratio plays a vital role in the development of the aluminosilicate gel. The Si/Al ratio for anorthite and mordenite at 45% was recorded between 2.68 and 3.80, and 2.34 to 6.12, respectively, whereas the Si/Al ratio of anorthite and mordenite phases at 55% of alkaline activators were between 2.48 and 2.88, and 2.33 to 4.88, respectively. Therefore, the higher Si/Al ratios (~3) are evident for anorthite in LSG at 45% of alkaline activator that corresponds to the higher dissolution of aluminosilicate to form C-(N)-A-S-H gel, thus the development of dense microstructure comparative to that of LSG at 55% of alkaline activator. Anorthite identified on mineral micrographs is classified as a calcium-rich aluminosilicate gel, whereas mordenite a sodium-rich gel N-(C)-A-S-H gel.

Based on the morphology and chemical composition of the geopolymer products, it can be deduced that a mordenite is an early form of aluminosilicate gel that has resulted soon after the partial dissolution of aluminosilicate, upon exposure to 45% of the alkaline activator, more dense aluminosilicate species develop with elemental composition matching with that of anorthite. Fig. 8b shows that at 45% of alkaline activator, the macro voids in anorthite were eliminated, while the microstructural morphology of mordenite at lower concentrations of alkaline activator appears porous at 35% of alkaline. Notably, after grinding and polishing the sample, the former mix displayed a smooth microstructure owing to its strong and dense microstructure. Also, due to its dense rheology, air bubbles can be seen entrapped in the microstructure while in the fresh state.

The distinction between C-(N)-A-S-H and N-(C)-A-S-H is drawn by comparing the Ca content in the mineral phases as shown in Fig. 9. The anorthite and mordenite phases presented in the TIMA micrograph are classified as C-(N)-A-S-H and N-(C)-A-S-H gel, respectively. Fig. 9 a, b, c, d represented the EDS spectral mapping of Ca, Na, mineral phases, and BSE micrograph of the $LS50FA50_{45}$ mix. The EDS spectral values of calcium (max spectral value 452) are comparatively higher than that of sodium, thus identified as anorthite on the BSE mapped micrograph. The calcium content has been contributed from the calcium-rich minerals such as calcite and gypsum in lithium slag, whereas aside from raising the alkalinity of the traces of sodium from the alkaline activator has also been chemically reacted with aluminosilicate aqueous phase as evident from the BSE mapped micrograph. The resulting anorthite-based aluminosilicate gel formed possessed gelling properties and encapsulated the lithium slag and fly ash particles, consequently attributing strength to the matrix.

The localized voids and cracks in LSG paste decreased with the increasing concentration of alkaline activator. Localized cracks that appeared could be thermal cracking that hasn't propagated in Fig. 10b and c. Higher alkaline activator content does not deleteriously affect the LSG, however, the higher concentration of alkaline activator above 45% affects the microstructure of LSG containing fly ash. This phenomenon is explained by higher cracking of aluminosilicate gel matrix at 55% of activator content marked by higher average crack width of fly ash incorporated LSG geopolymer paste at 55% activator content that possibly initiated due to thermal stresses during heat curing at 70°C because of higher dissolution of aluminosilicate. Similarly, the higher dissolution of aluminosilicate is evident in LSG from 45 to 55% of alkaline content, when the concentration of albite particles reduced from 34.09 to 27.05%, it raised the concentration of gelling species i.e. anorthite and mordenite from 31.61, 23.69 to 35.85, and 26.87% (Fig. 10b and c), respectively. Therefore, it can be deduced from TIMA analysis of LSG at varying alkaline activators that a higher concentration of alkaline activator increases the dissolution of aluminosilicate, thus reducing the overall porosity. However, in the case of fly ash incorporated LSG, higher dissolution of aluminosilicates is the function of compressive strength up to 45% alkaline activator, whereas beyond 45% the compressive strength decreased by thermal desiccation of aluminosilicate gel matrix as evident from Fig. 10a and b.

Alkali activation is the process of dissolving aluminosilicate from the surface of the minerals to form a monomer of aluminosilicates joining to form a long-chained polymer, called a geopolymer. The monomers of aluminosilicate attach with the alkali ions such as (Na^+, Ca^+, and K^+) to form a stable chemical composition [44,45]. The aluminosilicate gel was characterized stoichiometrically by mapping EDS spectra in automated mineral analysis (TIMA). The aluminosilicate minerals present in LSG were anorthite, albite, and plagioclase in lithium slag precursor, whereas the fly ash contains anorthite, albite, and mullite. The mixes contained 35, 45, and 55% of alkaline activators to dissolve aluminosilicates breaking the Si-O-Si and Al-O-Al bonds to form long linkages of Si-O-Al network stabilized by alkali cations such as Ca^+ and Na^+.

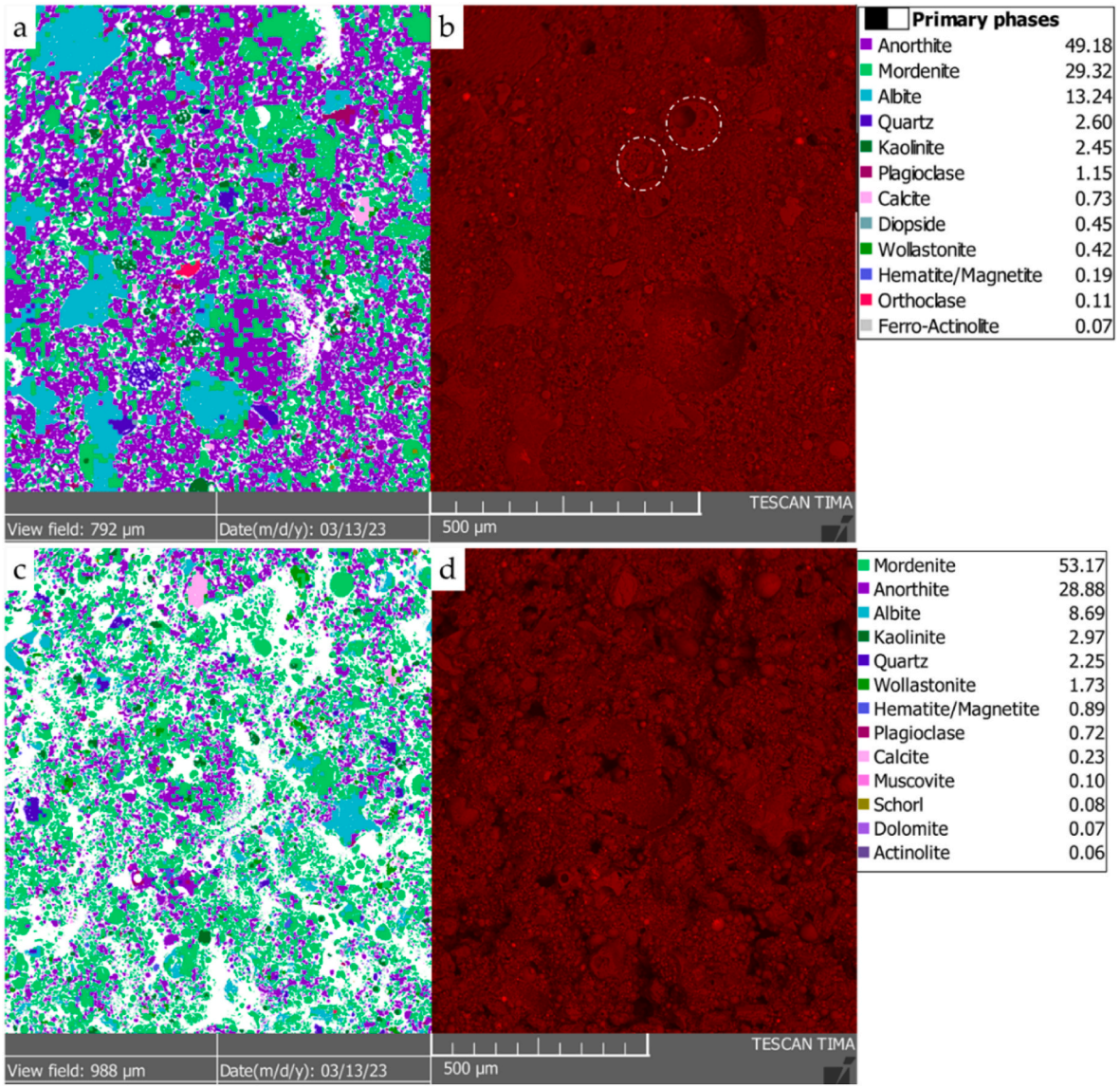

Fig. 8. Mineral phases and BSE micrographs of 50LS50FA at 45% (a, b) and 35% (c, d) of alkaline activator (Density of mordenite 2.1, anorthite 2.7, albite 2.6, kaolinite 2.6, and quartz 2.6) [18].

Mineral investigation reveals that the aluminosilicate gel shares chemical similarities with anorthite and mordenite, as seen in micrographs of their respective mineral phases. To characterize the ratio of their primary constituents, however, it is worthwhile to investigate the quality of anorthite and mordenite.

The Si/Al and Ca/Si ratios of the aluminosilicate gel were analyzed to evaluate the quality of microstructural development using TIMA. The identification of anorthite and mordenite phases as the primary aqueous phases in pore solution following the dissolution of aluminosilicates in LSG has been established from the microstructural morphology results. Fig. 11 depicts the microstructural composition of LSG under hydrothermal curing conditions (70°C) at 35, 45, and 55% of alkaline activator, as represented by the ternary plot of silica, alumina, and calcium oxides. The major aluminosilicate phases, including albite, anorthite, and mordenite, were characterized. In general, the albite phase exhibits partial reactivity post-geopolymerization, as indicated by Si/Al ratios that are relatively similar. At 45% of alkaline activators, there is a higher degree of variation in Si/Al ratio between 2 and 3 for the albite particles. However, the Si/Al ratio remains around 2.3 at both 35% and 55% of alkaline activator content. The anorthite and mordenite phases seem to have played a more significant role in geopolymerization, as evidenced by their Si/Al and Ca/Si ratio variations. As per the literature reference [46], it can be inferred that anorthite exhibits higher reactivity and experiences greater aluminosilicate dissolution at a pH above 11 and a curing temperature below 100 °C. Thus, it can be concluded that anorthite and mordenite play a dominant role in the strength development mechanism as C-(N)-A-S-H gel and zeolite, respectively. It is noteworthy to discover that the mordenite aqueous phase in the pore solution displayed comparable stoichiometric ratios to albite when subjected to a lower alkaline activator (35%). However, when the alkaline activator content was increased to 45%, significant changes in Ca/Si ratios were observed, and the average calcium content rose to 25%. This could potentially lead to the formation of aluminosilicate gel. The mordenite phase was formed through the dissolution of Ca-based minerals and aluminosilicates in the presence of a Na-based alkaline environment, resulting in the formation of a Ca, Na-based zeolitic microstructure (Na_2, $Ca)_4(Al_8Si_40)O_{96}.28H_2O$). The Si/Al ratios were found to be predominantly between 3.88 and 4.33 at 45% of alkaline activator. A smaller fraction of transformation from albite to mordenite was observed at 35 and 55% of alkaline activator content. In comparison to mordenite, anorthite exhibited a lower degree of variation in Si/Al ratios (ranging from 2.41 to 3.04) as the alkaline activator content was increased up to

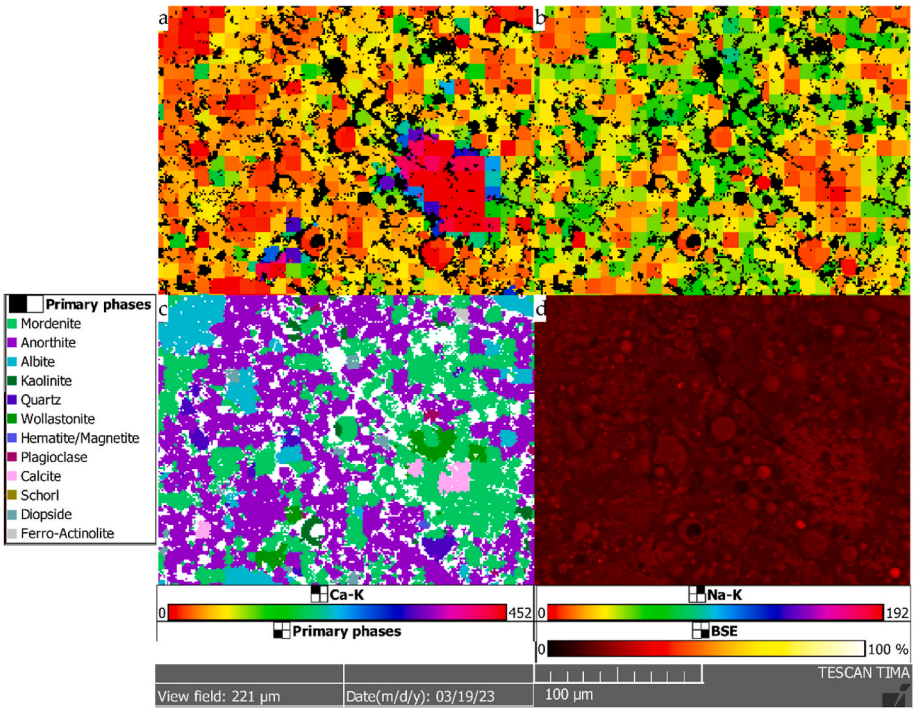

Fig. 9. EDS mapped spectral micrographs of 50LS50FA$_{45}$ geopolymer mix a) Calcium b) Sodium c) Primary phases (C-(N)-A-S-H gel/anorthite) d) BSE micrograph.

45%. However, the Si/Al ratios showed a significant variation at 55%. The mineral phases that exhibit distinct Si/Al ratios in specific areas indicate the development of fully matured aluminosilicate gel. Conversely, a significant fluctuation in Si/Al ratios indicates the presence of partially formed aluminosilicate gel. In examining the composition of mordenite and its physical characteristics, it is important to note that mordenite has a lower hardness value (3-4 on the Mohs hardness scale) compared to anorthite (6–6.5 Mohs hardness). Furthermore, it has been reported in previous studies that the highest strength of aluminosilicate is attained when the Si/Al ratio falls between 2.5 and 3 [36,37], therefore the composition of the C-(N)-A-S-H gel closely resembles the Si/Al ratio of anorthite. According to the Si/Al ratios observed in the C-(N)-A-S-H gel, it can be categorized as an intermediate calcium aluminosilicate gel [47]. Hence, the C-(N)-A-S-H gel represented by anorthite exhibits higher elastic modulus and hardness properties as compared to N-(C)-A-S-H gel represented by mordenite on mineral micrographs.

3.3. Micromechanical properties of LSG

The micromechanical properties, including elastic modulus and hardness, of LSG at varying alkaline activator concentrations and additive incorporation of fly ash and silica fume were determined using nano-indentation. The cyclic loading of the nano-indenter was applied on the surface features of the specimens to avoid overestimating elastic modulus and hardness values [48–51]. The modulus and hardness of the microstructural features have been mapped in a contour plot of data representing 100 data points on each specimen, and the microstructural phases were clustered and classified by the Probability Density Function (PDF) as unreacted particles of lithium slag, unreacted quartz particles, anorthite, and mordenite while investigating elastic modulus in conjunction with the mineral phase micrographs (Fig. 12-a, c, e). The nanoindentation test was used to evaluate the load-displacement behavior of each phase, including partially reacted lithium slag and silica fume. The results presented the indentation of the Berkovich indenter upon 100 different locations of the 200 × 200 µm^2 grid, in which each tested point was separated by 20 µm for capturing a larger area for analysis and to ensure sufficient data points representing each involved phase's load-displacement behavior. The micromechanical investigation of the LSG paste matrix was performed by both quantitative analysis and qualitative analysis.

3.3.1. Quantitative analysis

To better understand the micromechanical properties of the LSG paste, the phase properties were determined by the statistical Gaussian deconvolution technique. Clusters of data with distinct micromechanical properties can be identified using the Gaussian deconvolution approach [52]. Fitting the experimental data, deconvoluting the Gaussian distribution, identifying the phases, and analyzing the data are the four steps involved in determining the elastic moduli of different phases. The experimental data is expressed in terms of elastic modulus, and the PDF is first fitted to the frequency density (normalized histogram with a bin size of 3 GPa). Using the Shapiro-Wilk test, it was found that the experimental PDF of constituent phases follows a normal distribution, it can also be assumed as per literature [52,53]; as a result, the theoretical PDF for the experimental data by deconvolving the experimental PDF using the Gaussian distribution curves were derived which are shown in Fig. 12 and the gaussian deconvolution results are reported in Table 4. Microstructural and mineral phase identification studies establish the number of Gaussian distribution curves (section 3.2). N-(C)-A-S-H (mordenite), C-(N)-A-S-H (anorthite), partially reacted LS particle, and silica particle are the four phases identified. Micromechanical characteristics (elastic modulus) were used to categorize these stages, after which gaussian deconvolution was performed. When ground furnace slag and fly ash are mixed, they create six phases, two of which are N-A-S-H and C-A-S-H, with elastic moduli in the order N-(C)-A-S-H (mordenite) < C-(N)-A-S-H (anorthite) < partially reacted LS particles < silica particles [54,55].

The micromechanical moduli were characterized using PDF. In LSG with a 45% alkaline activator, a first frequency distribution peak for anorthite (62%) was observed, along with peaks for mordenite (14%), and partially reacted LS particles (24%). After clustering of elastic moduli as per PDF and corresponding hardness values, the elastic modulus of mordenite resulted as 19.01 GPa, which is lower than that of

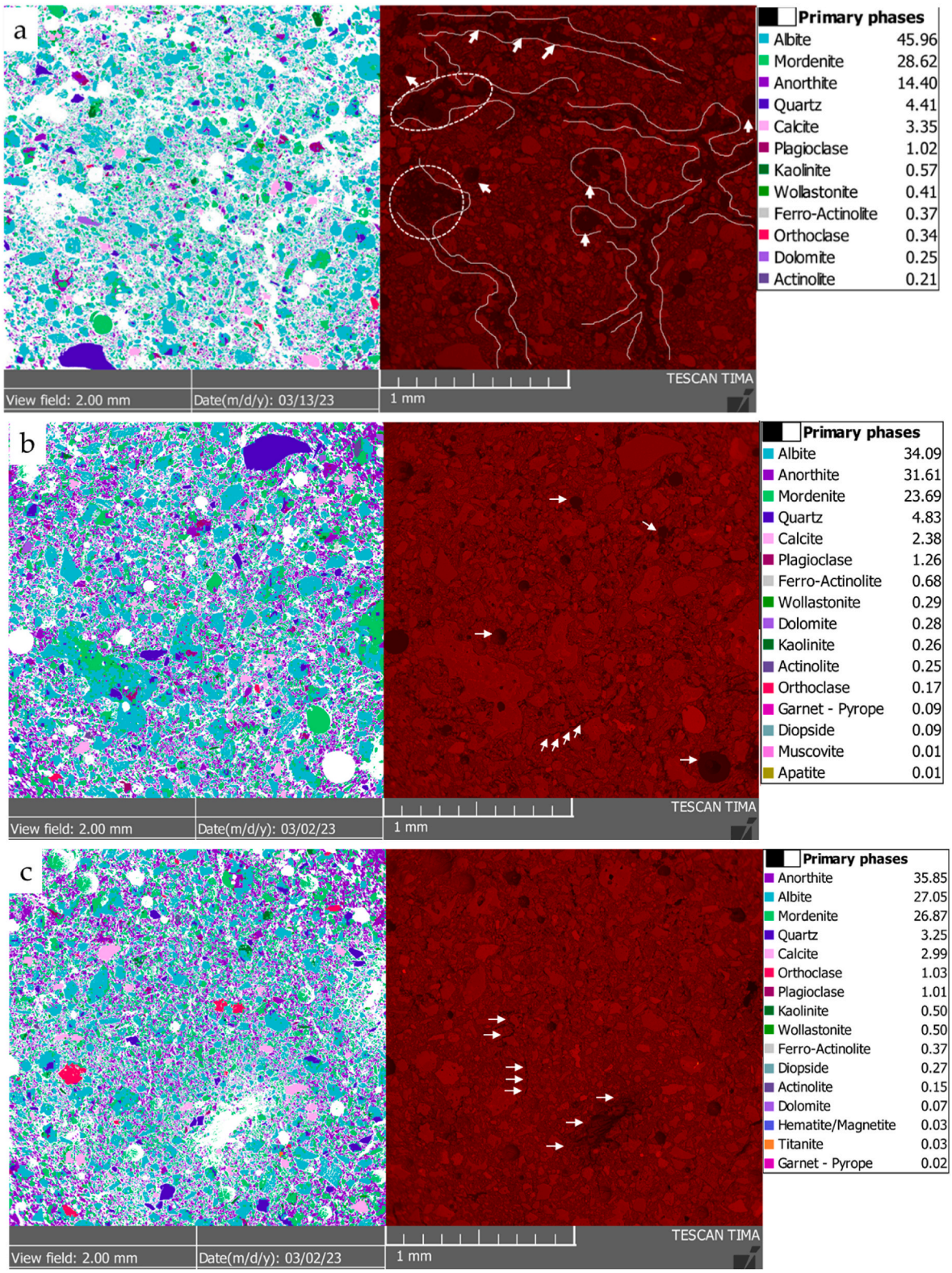

Fig. 10. The mineral phases of LSG containing a) 35% [18] b) 45% c) 55% of activator.

anorthite (22.54 GPa) and partially reacted particles (29.20 GPa) [56, 57]. Mordenite, on the other hand, accounted for 41% of the frequency distribution, anorthite 34%, partially reacted LS particles 19%, and unreacted particles 10% of the alkaline activator concentration. The anorthite-based aluminosilicate concentration dropped significantly at 55% alkaline activator, and the mordenite phase's lower elastic moduli values caused the microstructure to weaken. Also, as shown in Fig. 12c, at 55% alkaline activator, the percentage of partially reacted LS particles was higher. We were able to determine a 46% frequency distribution of mordenite in the silica fume containing LSG, 32% aluminosilicate as anorthite phase, 16% partially reacted lithium slag, and 5% partially reacted silica particles based on the elastic modulus values. The elastic

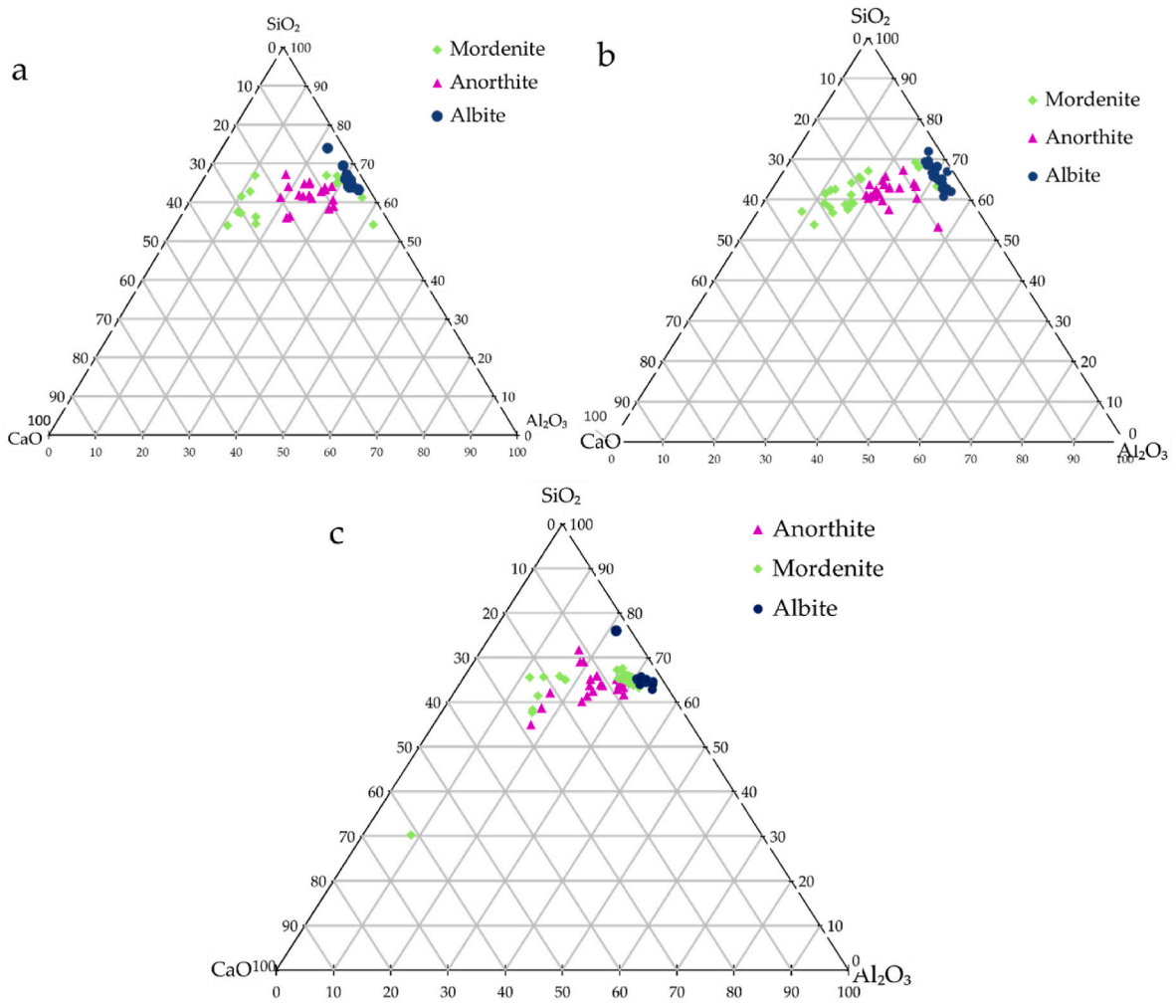

Fig. 11. Ternary graph of LSG at 35, 45, and 55% of alkaline activator.

modulus of mordenite, anorthite, partially reacted lithium slag, and silica fume were 15.49, 17.80, 20.96, and 21 GPa, which are similar to that reported in the literature [56,57]. The elastic modulus of silica fume-incorporated geopolymer appeared to be less affected by aluminosilicate dissolution. According to mineral analysis, the majority of the aluminosilicate particles that dissolve into the geopolymer paste matrix and produce the aluminosilicate pore gel are C-(N)-A-S-H (Si/Al~3) and N-(C)-A-S-H (Si/Al~6) gels. Therefore, the variation of elastic moduli at different alkaline activators is due to the degree of dissolution of aluminosilicates from the precursor minerals which is a function of alkalinity of alkaline activator solution. The moduli values were observed higher at Si/Al ratio between 2.41 and 3.04, whereas Si/Al ratio between 3.88 and 4.33 represents lower dissolution of aluminosilicates. Literature has suggested the effectiveness of nanoindentation for determining and correlating micromechanical properties with compressive strength. Luo et al. [58] investigated the micromechanical properties of fly ash incorporated geopolymer containing silica and nano titanium oxide. The results reported that the nanoparticles, especially nano-titanium oxide, have stronger mechanical qualities than gel particles but less percentage. Nano-SiO_2 disperses and bonds better with sodium silicate solution and gel particles. Geopolymer containing nano-silica is stronger than geopolymer containing nano-titanium. In another study, Luo et al. [59] also investigated the properties and heterogeneity ITZ in geopolymer and consequently reported the characteristics and variability. An approach for examining more complex ITZs is proposed, and it is shown that the ITZs at the top and bottom borders have superior qualities than those at the lateral boundaries and bulk paste.

Conclusively, PDF analysis was used to evaluate the micromechanical moduli of distinct phases in a range of LSG samples. The findings revealed that mordenite's elastic modulus values were lower than those of anorthite and partially reacted LS particles. At 55% alkaline activator, the microstructure relatively weakened due to a drop in C-(N)-A-S-H gel concentration and a rise in mordenite and partially reacted LS particles. Particles of mordenite, anorthite, and partially reacted LS were found in addition to partially reacted silica particles in LSG that contained silica fume. Conclusively, the microstructure was found to be weakened by the lower elastic moduli values of the mordenite phase at higher concentrations of alkaline activators. However, the geopolymer containing silica fume exhibited a lower susceptibility toward the formation of mordenite and weaker microstructure.

3.3.2. *Qualitative analysis*

The grid nano-indentation approach was used to qualitatively assess the strength of the aluminosilicate gel phases and partially reacted particles. The mechanical properties, such as elastic modulus and hardness, were determined by analyzing the load-displacement relationship. The elastic moduli of the phases were determined by the slope of the unloading curve, using the contact mechanics approach using the Oliver Pharr method of analysis [51,60]. Because plastic deformation and indenter geometry can affect the slope of the loading curve, it is not used in the calculation of elastic modulus [28].

Fig. 13 shows the load-displacement curves of LSG containing silica fume mix containing reaction products and unreacted particles, whereas

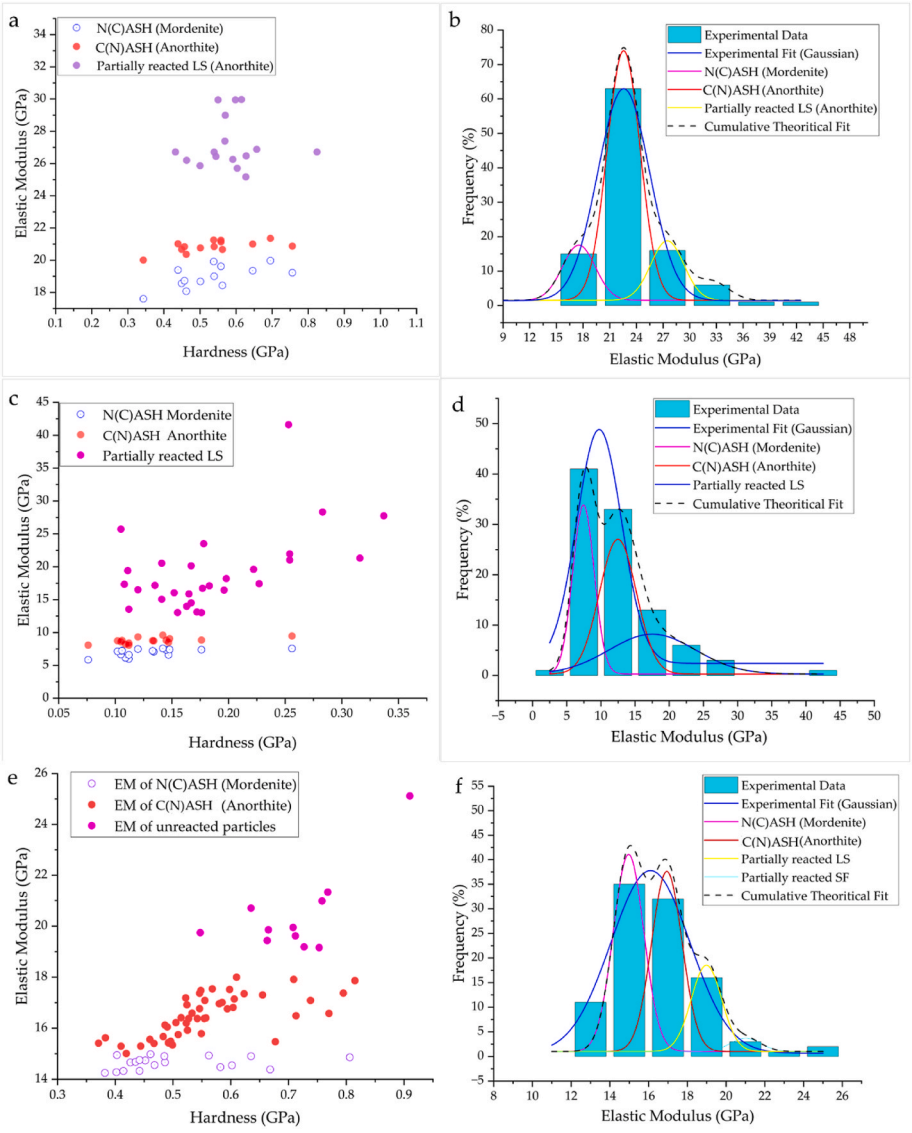

Fig. 12. Gaussian deconvolution of elastic modulus of LSG at 45% (a, b) and 55% (c, d) of alkaline activator, and LSG mix containing 40% silica fume (e, f).

Table 4
Gaussian deconvolution of lithium slag particles and aluminosilicate phases in LSG.

Sr. No	Phases	Symbols	LSG (45%)	LSG (55%)	60LS40SF$_{45}$
1	N-(C)-A-S-H gel (Mordenite)	Mean (μ) ± SD (σ)	19.01 ± 0.67 (14%)	6.95 ± 0.55 (41%)	15.49 ± 0.81 (46%)
2	C-(N)-A-S-H gel (Anorthite)	μ ± σ	22.54 ± 1.20 (62%)	10.35 ± 1.42 (34%)	17.80 ± 0.57 (32%)
3	Partially reacted LS	μ ± σ	29.20 ± 3.69 (24%)	19.17 ± 4.16 (19%)	20.96 ± 1.97 (22%)

unreacted particles represent the silica fume and lithium slag unreacted particles. The difference in the maximum load and unloading slope of the individual phases corresponds to the elastic moduli values [61]. The displacement of partially reacted lithium slag particles is lower than that of aluminosilicate products and the slope of the initial unloading portion of load-displacement is generally higher than that of aluminosilicate reaction products. Therefore, the order of the elastic modulus is mordenite (N-(C)-A-S-H) < anorthite C-(N)-A-S-H) < lithium slag < silica fume. Mordenite has the highest values of displacement (5.50 μm), followed by anorthite (6.05 μm), and least reported for unreacted particles (7.05 μm). From the literature [51,62,63], it is evident that the higher elastic materials have a higher slope of the load-displacement curve. Although unreacted particles of lithium slag and silica fume have higher elastic moduli values in the geopolymer paste matrix, the strength of LSG is governed by the elastic moduli of dissolved aluminosilicates such as anorthite and mordenite, encapsulating the unreacted particles which were generated as a result of geopolymerization.

The contour mapping of elastic modulus and hardness of the LSG at varying alkaline (45 and 55%) activator content and silica fume incorporated mixes are presented in Fig. 14 a-b, c-d, and e-f, respectively. These values of moduli are shown in terms of the degree of darkness of cyan, green, and red colors on the micromechanical moduli contour map. The red area shows the moduli of unreacted lithium slag particles, the green area shows the partially reacted lithium slag particles, and the area covered by cyan refers to amorphous aluminosilicates produced as a result of geopolymerization (chemical composition similar to anorthite, but with higher Si/Al), and blue area refers to the moduli of mordenite. While comparing LSG at 45 and 55% of alkaline activator, its hardness at 45% of alkaline activator has higher values than later mix,

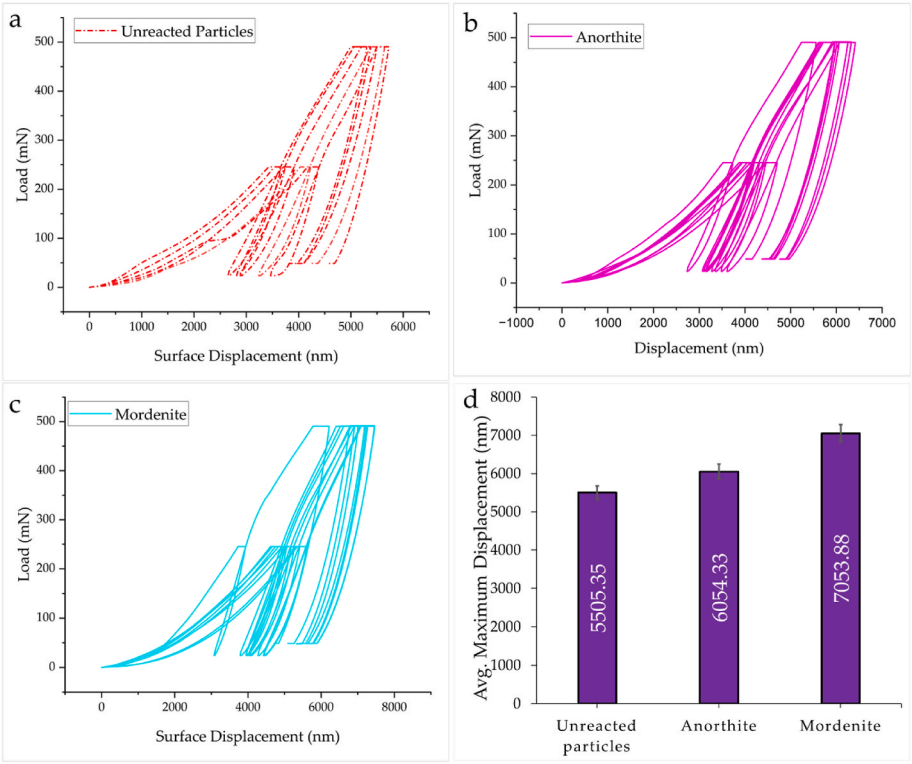

Fig. 13. Micromechanical characterization of phases by cyclic loading on nano-indentation of silica fume incorporated LSG.

marked by over 70% area covered by anorthite and partially reacted LS particles, and the least area was covered by mordenite, whereas the average modulus values shown in anorthite, partially reacted particles, and mordenite phases are 22.80, 27.58, and 18.98 GPa respectively. Contrarily, the larger blue area (7.79 GPa) representing the mordenite in LSG in a 55% alkaline activator LSG mix displayed lower values of moduli compared to both the anorthite phase with a modulus of 11.78 GPa and partially reacted LS particles with a modulus of 17.76 GPa. In addition, the overall moduli of the microstructural paste matrix are lower in LSG containing 55% of alkaline activator than it is in LSG containing 45% of the activator, which demonstrates that LSG at 55% has a lower micromechanical strength.

Table 5 shows the statistical significance of elastic modulus values of geopolymer mix phases, which was determined by ANOVA analysis. This approach compares the probability value (P-value) against the significance threshold to determine if the observed groups differ [64]. The significance threshold is usually 0.05 [65]. If the P-value is below 0.05, the observed groups differ significantly. Otherwise, the observed groups exhibit no significant difference (P-value >0.05). If the P-value is below 0.01, the observed groups vary strongly.

The ANOVA analysis compares the means of three or more groups to see if they are substantially different. In this scenario, the three groups are A: Mordenite, B: Anorthite, and C: partly reacted particles, and the geopolymer mixtures are 100LS0FA-45, 55, and 60LS40SF. The stronger the F-value, the greater the gap between the groups' means. A small p-value implies strong evidence against the null hypothesis (that the means are equal) and suggests that the means differ significantly. Hence, Table 5 shows that for all geopolymer blends, the mean elastic modulus values of the three phases differ significantly.

3.4. Nanostructure of C-(N)-A-S-H gel

The nanostructure and crystallographic phases of LSG containing silica fume were identified, and its nano-morphology of aluminosilicate gel was determined by STEM and SAED which is shown in Fig. 15.

The development of aluminosilicate gel characterized at the nano-scale is presented in the bright-field image in Fig. 15a. The mordenite particles, which are partially reacted lithium slag, undergo further geopolymerization to form an aluminosilicate gel with a foil-like structure. The mordenite particles with a Si/Al ratio greater than 5 underwent partial dissolution of aluminosilicate and resulted in the formation of C-(N)-A-S-H gel. The gel had a Si/Al ratio of 3.48 and a Ca/Si ratio of 0.33, which is shown in Table 6. The mapping of bright field images and EDS spectra indicate the decrease in Si/Al upon geopolymerization, as shown in line EDS (Fig. 15a), which results in the formation of an aluminosilicate gel that surrounds the lithium slag particles. The nano-structure of C-(N)-A-S-H gel is amorphous in nature. Despite having a lower elastic modulus than lithium slag particles, it plays a crucial role in determining the strength of LSG. According to the Gaussian deconvolution of elastic modulus, the geopolymerization reaction products in LSG containing silica fume can be arranged in descending order of elastic modulus as; Partially reacted particles > C-(N)-A-S-H gel (anorthite) > N-(C)-A-S-H gel (mordenite). The average values along with the standard deviation of elastic modulus for these products were found as 20.96 ± 1.97, 17.80 ± 0.57, and 15.49 ± 0.81 GPa, respectively.

The SAED pattern of aluminosilicate gel exhibits a combination of mineral phases, including anorthite, mordenite, quartz, and calcite, as observed in High-Resolution Transmission Electron Microscopy (HRTEM) images. The pattern is amorphous, and polycrystalline in nature, and it is pertinent to mention that all the aforementioned crystals exhibited an amorphous nature, coexisted within the same microstructure, and were comprised of aluminosilicate gel except calcite. The identification of mineral phases was achieved through the determination of interplanar spacing (d-values) by measuring the radius of halos for amorphous minerals and the atomic distance from the center of bright source X-ray for crystalline minerals which are reported in Table 7. Anorthite was detected at d-values of 2.69, 2.36, 1.88, and 1.14 Å, quartz was observed at 1.18 Å, mordenite at 1.60 Å, and calcite at 1.92 and 3.01 Å. The d-values were validated through Rietveld refinement of the modeled phases, and the stated minerals were quantified as

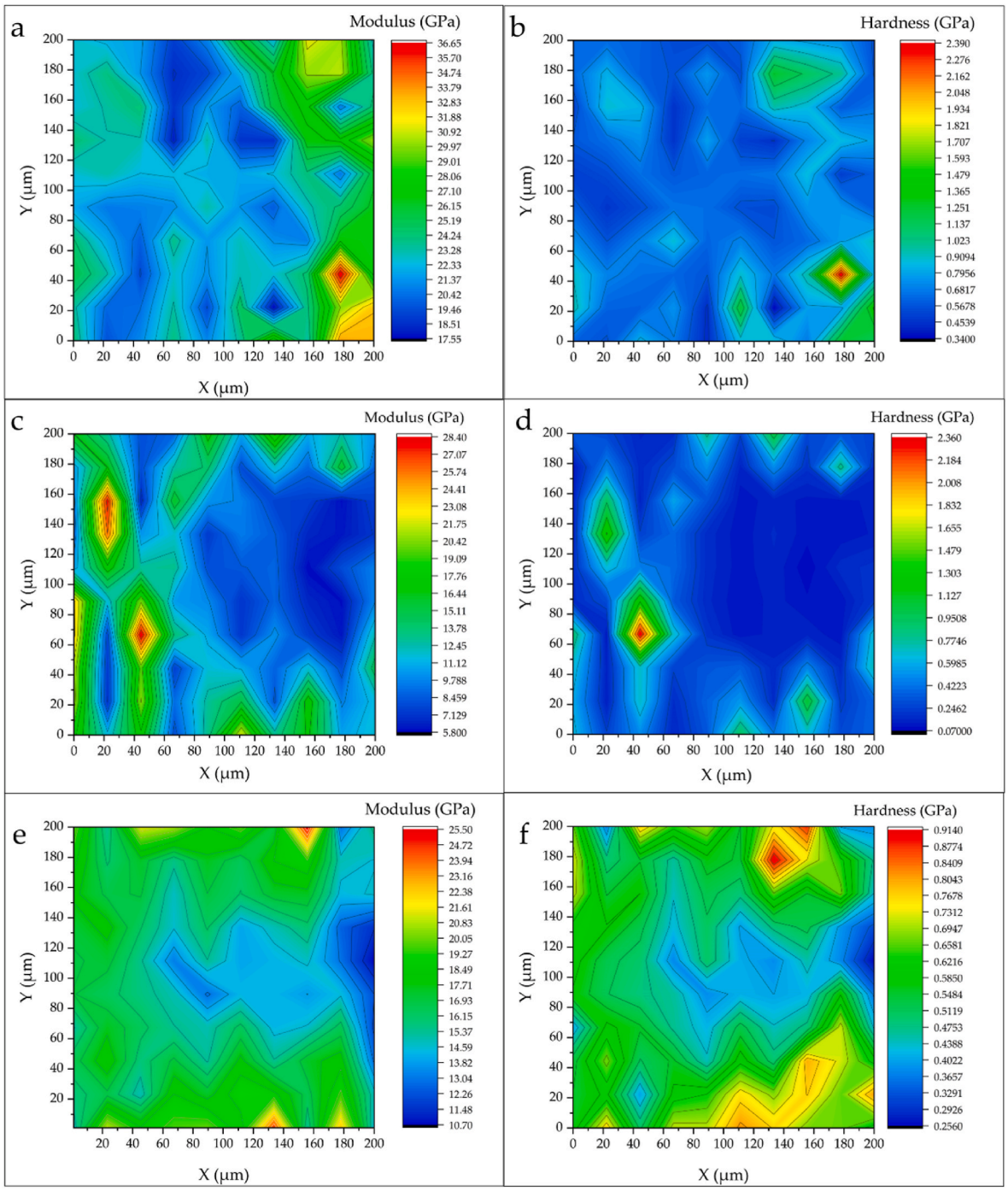

Fig. 14. Hardness and elastic modulus at constant force of 580 mN; a, b) 100LS0FA$_{45}$ c, d) 100LS0FA$_{55}$ e, f) 60LS40SF$_{45}$.

well. It is noteworthy to state that geopolymerization leads to the formation of amorphous chained polytetrahedrons consisting of covalently bonded oligomers of aluminosilicates. The strength of these oligomers is impacted by the quantity of silica, alumina, and activator concentration present in the reactants. The nano-silica particles that may have originated from the carbonation reaction (Fig. 15e), significantly contributed toward the formation of aluminosilicate gel at the later stage of strength development and enhanced the dissolution of aluminosilicate. The interconnected reactive silica particles exhibit a spherical morphology, with a diameter of 50 nm for each nano-silica particle. These particles possess the ability to dissolve in aluminosilicate gel more readily than the micro-sized silica fume particles. Thus, the SAED analysis indicated the generation of an amorphous aluminosilicate gel and the formation of crystalline calcite after geopolymerization.

In addition to the amorphous gel morphology, the aluminosilicate gel exhibits the presence of calcite crystals with a rhombohedral lattice structure depicting the occurrence of carbonation, as depicted in Fig. 15 d, e. The process of carbonation entails the penetration of carbon dioxide into the pores of the geopolymer, which is then followed by the carbon dioxide's dissolution with a water molecule, thereby producing carbonic acid. The carbonic acid subsequently undergoes a reaction with sodium silicate, resulting in the generation of sodium carbonate and silicic acid. Ultimately, the chemical reaction between sodium carbonate and calcium hydroxide yields sodium hydroxide and calcium carbonate as shown in Eq. (3). The mechanism is briefly expressed by Eqs. (2)–(4).

Table 5
Statistical significance of elastic modulus values of LSG mixes, A: Mordenite (N-(C)-A-S-H), B: Anorthite (C-(N)-A-S-H), C: partially reacted particles (*lower p-values indicate the mean elastic moduli values are significantly different).

Geopolymer mixes	Group	F-value	p-value*
$100LS0FA_{45}$	A&B	108.35	3.82×10^{-16}
	B&C	154.44	9.98×10^{-21}
	A&C	99.17	6.93×10^{-12}
$100LS0FA_{55}$	A&B	83.42	5.07×10^{-13}
	B&C	93.64	8.86×10^{-15}
	A&C	65.41	3.55×10^{-10}
$60LS40SF_{45}$	A&B	82.34	5.66×10^{-14}
	B&C	157.20	6.79×10^{-18}
	A&C	90.41	4.45×10^{-13}

$$CO_2 + H_2O \rightarrow H_2CO_3 \quad (2)$$

$$H_2CO_3 + Na_2SiO_3 \rightarrow Na_2CO_3 + H_2SiO_3 \quad (3)$$

$$Na_2CO_3 + Ca(OH)_2 \rightarrow CaCO_3 + 2NaOH \quad (4)$$

The wide range of calcite distribution within microstructures is widely observed across various crystal orientations, as illustrated in Fig. 15d. This indicates that the microstructure exhibits a higher concentration of calcite, which is associated with a higher level of carbonation. The possible formation of calcite is ascribed to the carbonation phenomenon occurring in LSG containing silica fume and this phenomenon is less pronounced in fly ash incorporated LSG as the lower calcite formation reported in authors' previous research of similar geopolymer paste matrix [18]. The release of Ca^{+2} ions upon exposure to the environment is a critical factor in the carbonation of geopolymer, particularly concerning the dissolution of calcium-bearing species such as anhydrite in an alkaline environment. The obtained SAED results from the area of interest indicate the formation of calcite within the compacted LSG matrix that has been added with silica fume. The process of carbonation of Ca-aluminosilicate gel in the pore solution resulted in the formation of calcite and silica particles. These calcite crystals and silica particles formed have been depicted in the HRTEM image (Fig. 15d and e) which has also been reported in previous studies [66,67]. The elemental spectral micrographs of LSG containing 0 and 40% silica fume are shown in Fig. 15f, representing the suppressed formation of calcic species due to carbonation in the microstructure at higher silica fume content. The carbonation-induced deterioration has been presented on EDS spectral micrographs of Ca and C elements indication the concentration of $CaCO_3$ in spatial resolution. The higher concentration of carbonation products is shown by higher spectral values indicating a higher level of cracking and porous microstructure marked by epoxy-filled dark regions in spectral micrographs. The deteriorated effect of carbonation in 0% silica fume LSG specimen is dominated and underwent significant cracking, the deteriorated regions are encircled in the micrographs and appeared to be higher in EDS spectral value for Ca and C. Comparatively lesser cracking was observed in the 40% silica fume incorporated than that of the 100LS0SF LSG mix marked by a relatively lower concentration of carbonation products as revealed by lower EDS spectral values of Ca and C. Therefore, carbonation product generation was suppressed upon incorporation of silica fume but still exists in LSG containing 40% silica fume.

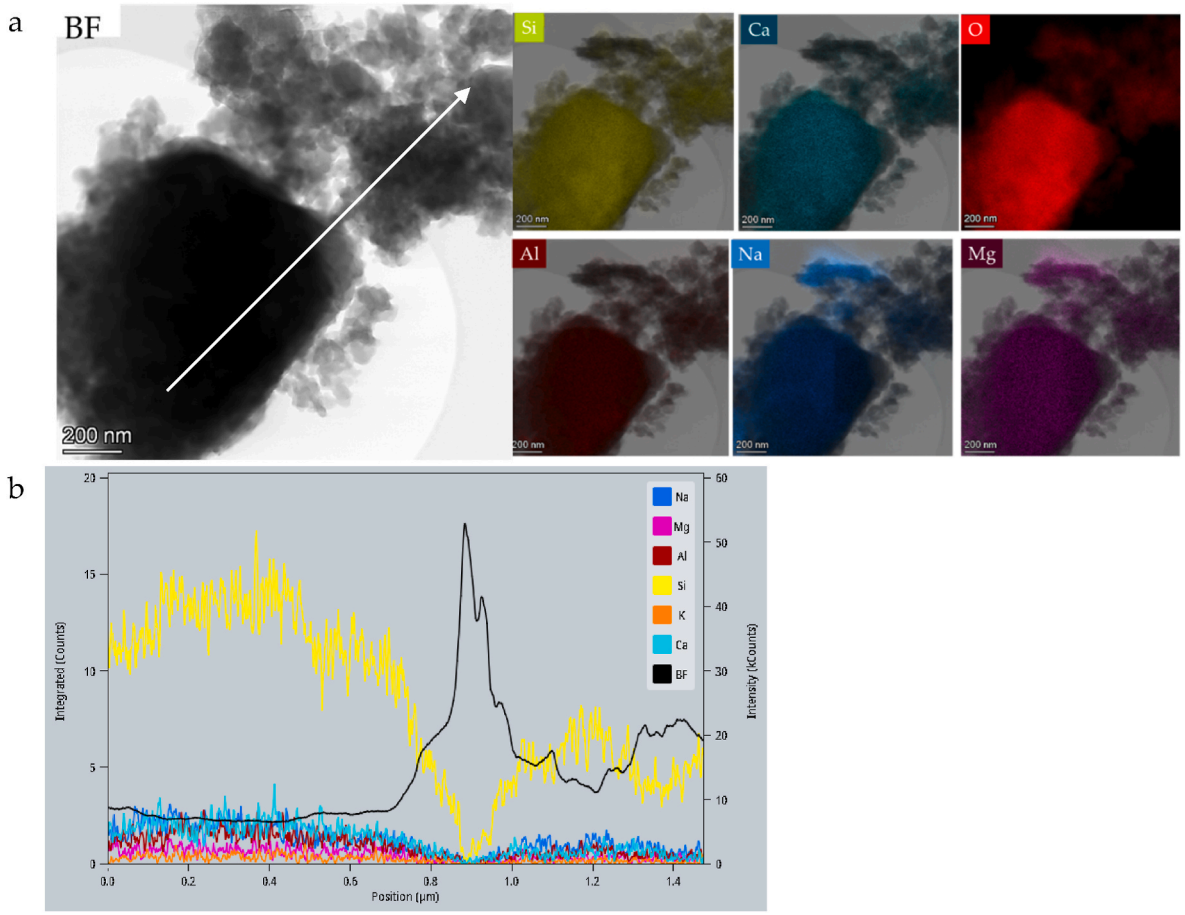

Fig. 15. STEM of $60LS40SF_{45}$ a) Nano-structural development of C-(N)-A-S-H gel, b) Mapping of line EDS elemental spectra of aluminosilicate gel, c) HRTEM and SAED patterns of aluminosilicate gel, d) SAED of rhombohedral lattice system (Calcite), e) Partially reacted silica fume nano-particles, f) Elemental spectra micrographs of LSG depicting the deteriorated regions by carbonation.

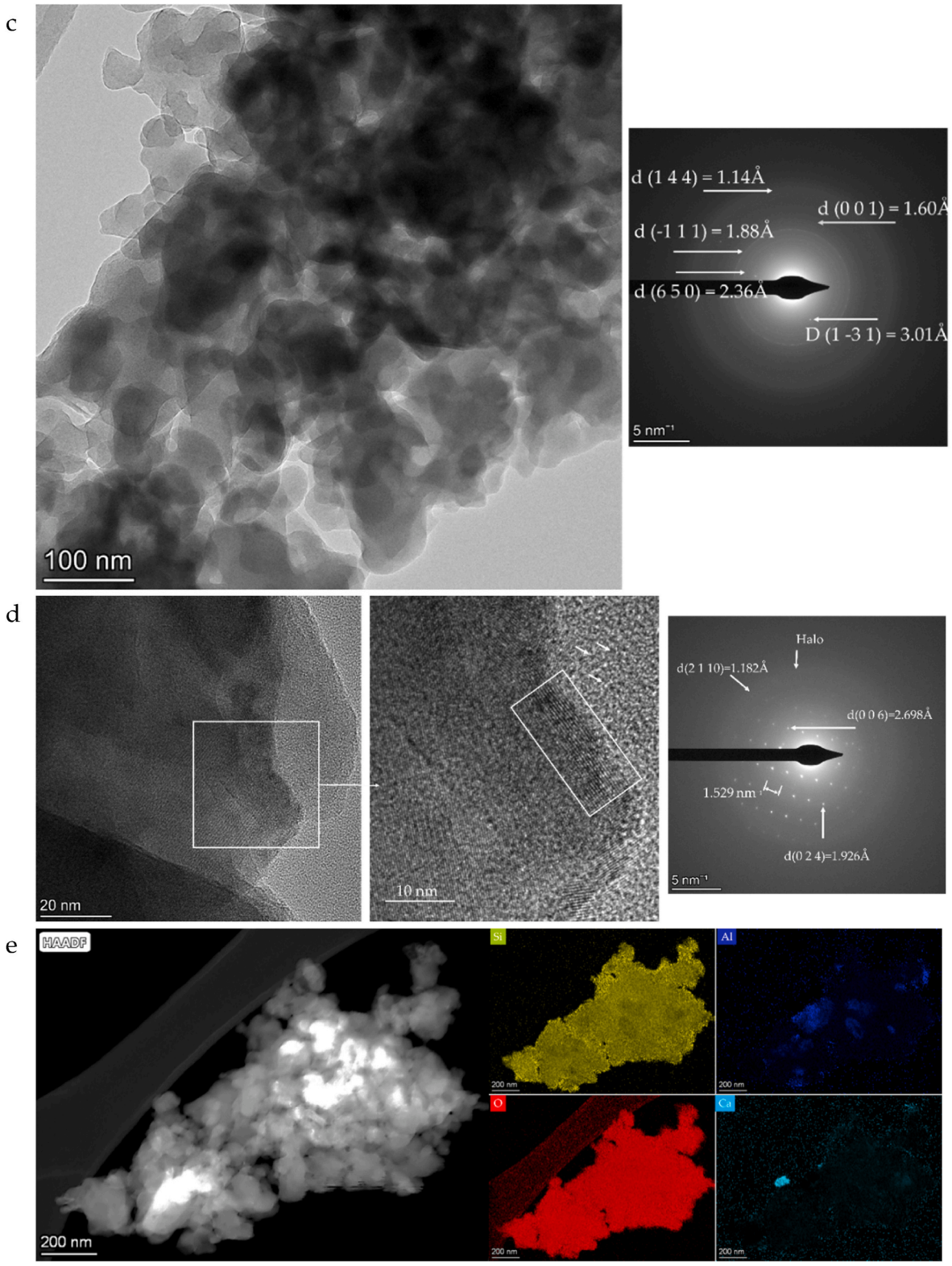

Fig. 15. (*continued*).

Similar results were reported in the literature [68], in which carbonation products and aluminosilicate gel generated spontaneously till an extended period of curing, thus resulting least deterioration in strength. Nevertheless, the effect of carbonation on strength and durability properties is dependent on various factors such as types of precursors, alkaline activators, and carbonation conditions, thus the results of carbonation varied significantly by changing these factors as per the published literature [69–72]. These properties could potentially reduce the durability of the microstructural composition by lowering pH and increasing the porosity of the geopolymer [73,74]. Upon exposure to carbon dioxide in the atmosphere, the calcium ions present in the pore solution of LSG engage in a reaction with carbonate ions resulting in the

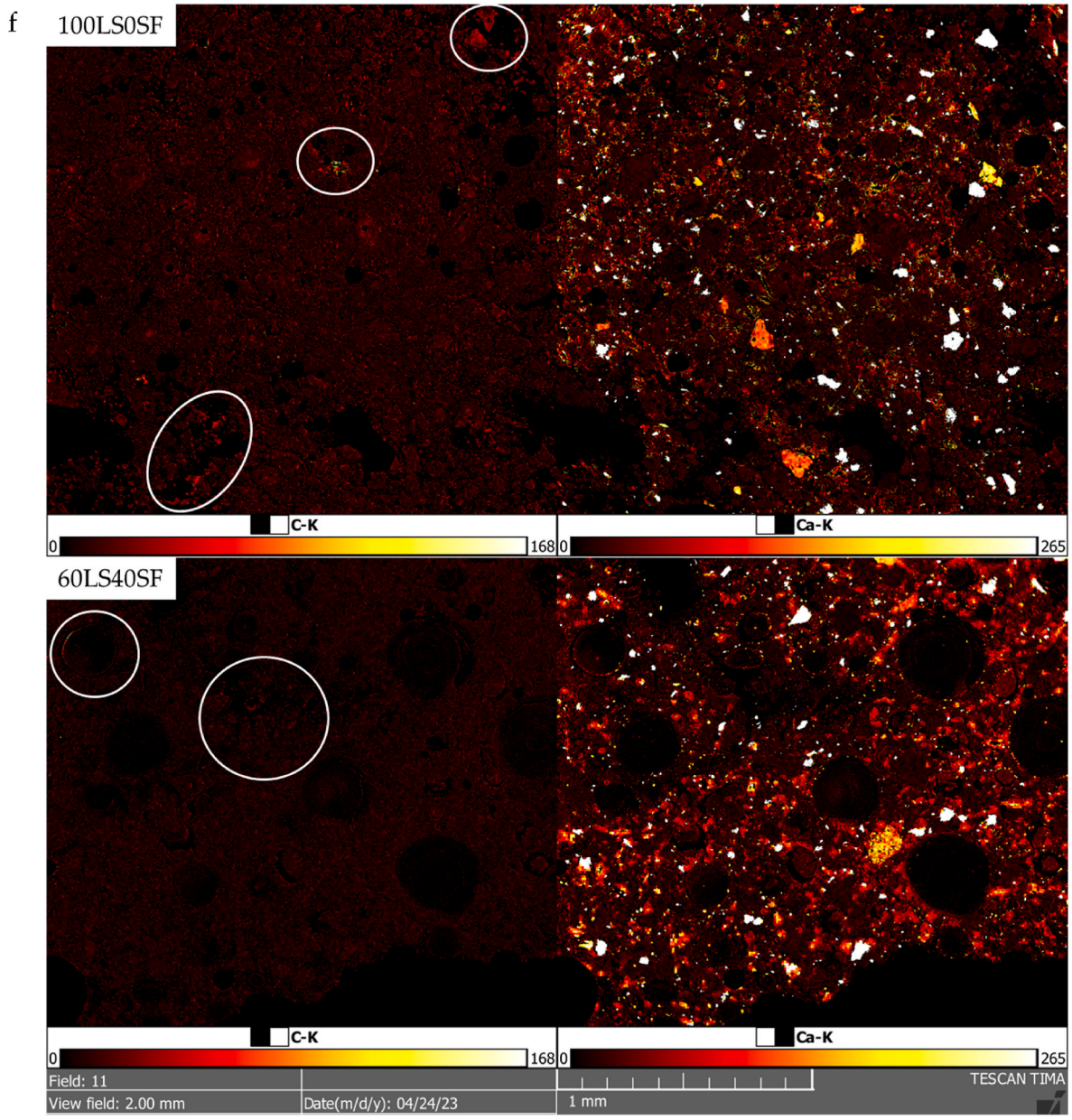

Fig. 15. (*continued*).

Table 6
Elemental composition of C-(N)-A-S-H gel on Bright Phase-image (From Fig. 15a).

Element	O	Na	Mg	Al	Si	Ca	K	Si/Al
Percentage	59.48	4.09	2.11	6.07	21.16	6.06	1.03	3.48

Table 7
Crystal phases identification by SAED patterns in STEM.

1/r (1/nm)	d (nm)	d (Å)	hkl	Mineral phases
8.45325	0.118298	1.182977	(2 1 10)	Quartz
5.19	0.192678	1.926782	(0 2 4)	Calcite
3.706	0.269833	2.698327	(0 0 6)	Calcite
4.22675	0.236588	2.365884	(6 5 0)	Anorthite
5.2965	0.188804	1.888039	(3 2 2)	Anorthite
6.243	0.160179	1.601794	(6 0 4)	Mordenite
8.77125	0.114009	1.140088	(6 3 -10)	Anorthite
3.316	0.301568	3.015682	(1 -3 1)	Calcite

formation of calcite [75]. Simultaneously, the aluminosilicate gel present in LSG undergoes dissolution and releases silica, which subsequently forms silica gel. The process of nucleation of silica nano-particles takes place close to the calcite formation, leading to the formation of a highly ordered structure [76]. Therefore, the overwhelming evidence of carbonation in LSG has been revealed from the results of SAED, and mineral analysis of LSG paste matrix.

3.5. Rietveld quantitative analysis

The mineral peaks were modeled and quantified using the double-Voigt approach for better fitting accuracy, reliability, and physical

significance of Rietveld refinement [77]. The percentage of mineral phases in LSG containing 40% of silica fume including quartz, calcite, anorthite, mordenite, spodumene, and albite as 29.59, 19.90, 8.20, 7.13, 4.70, and 4.05%, respectively are shown in Fig. 16. The calcite phase in the LSG specimen at 45% of the alkaline activator is 19.90% which is around two times higher than the LSG containing silica fume at 35% of the alkaline activator as reported in the literature [18]. Alkali activation led to the formation of aluminosilicate gel as well as a higher calcite content in the matrix of the geopolymer paste which resulted because of carbonation. Numerous research studies [78,79] have found overwhelming evidence of the formation of calcite polymorphs like calcite, vaterite, and hydrotalcite. However, according to the Rietveld analysis, calcite is the only carbonation product found in LSG that contains silica fume, which is consistent with the findings given by Bernal et al. [69], which increased the carbonation upon incorporation of metakaolin in geopolymer. The published literature [80–82] has also revealed the formation of calcite in the geopolymer paste matrix. The micro-sized calcite particles could improve microstructure by pore refinement on one hand and lower the pH, consequently decalcifying aluminosilicate gel and causing autogenous shrinkage. The net-effect of carbonation reported in literature could induce porosity and lower the strength. Therefore, the carbonation is minimal at 40% replacement of silica fume, thus decreasing porosity and densifying the microstructure of the LSG paste matrix.

3.6. Compressive strength

Compressive strength is an essential macro-mechanical property of geopolymer that determines its durability and longevity. The compressive strength of LSG containing 45 and 55% of alkaline activator and additive incorporation of fly ash is shown in Fig. 17.

The compressive strength of LSG without fly ash at 45% alkaline activator showed a relatively low strength gain between 7 and 28 days, with only a 3.86% increase in strength (Fig. 17a). However, the addition of fly ash as a partial replacement for lithium slag resulted in a significant improvement in compressive strength, with a 4.67 times increase in strength at 28 days compared to the reference mix (100LS0FA). The 55% activator content also contributed to the higher strength gain, with a 30.37% increase in strength at 28 days compared to the 45% activator content. The compressive strength of LSG containing 50% fly ash revealed significant improvement between 7 and 28 days, with a 13.86% increase in strength. The addition of fly ash as a partial replacement of lithium slag resulted in a 1.13 times higher compressive strength at 28 days compared to the reference mix (100LS0FA). The 55% activator content also contributed to the higher strength gain, with a 31.97% increase in strength at 28 days compared to the 45% activator content. The existence of alumina and silica in stable compounds such as spodumene, anorthite, and albite accounts for the suppressed performance of lithium slag in geopolymer [18]. Fly ash, on the other hand, contains more reactive forms of silica and alumina in the form of quartz and mullite, respectively [4,83,84], which are more reactive. Hence, the compressive strength is increased by using fly ash in place of some of the lithium slag. The LSG containing 20% silica fume resulted in a 17.64% increase in compressive strength between 7 and 28 days, and 39.77% of strength development was recorded by incorporating 20% silica fume which increased to 50.49% upon further 20% replacement of lithium slag with silica fume (Fig. 17c). The strength development of LSG containing 40% of silica fume showed a strength development of 17.81% at 28 days of curing.

Fig. 17d reveals the strength development trends at higher alkaline activators, which are worth discussing from the perspective of the degree of dissolution of aluminosilicates in the geopolymer paste matrix. The compressive strength of 50% incorporated fly ash LSG increased significantly by increasing the percentage of alkaline activator in geopolymer paste composite. The compressive strength of LSG containing a 35% alkaline activator was taken from the authors' previous study of lithium slag for comparison purposes [18]. The compressive strength of LSG at 40% of alkaline activator increased to 2.52 times higher than that reported before, whereas 34.35% of the increase in compressive strength was recorded at 45% of alkaline activator. The manifold increase in compressive strength upon a higher alkaline activator is due to the higher dissolution of aluminosilicate from lithium slag and fly ash [85–87]. The increase in strength over time can be attributed to the ongoing reactions between the geopolymer and the curing environment. These reactions include the hydrolysis of the aluminosilicate precursor and the condensation of the resulting silanol groups, leading to the formation of a crosslinked network and thus an increase in strength [88,89]. Similarly, various research studies have reported increased compressive strength by increasing the concentration of alkali ions [90–92]. Additionally, the curing environment plays a role in the strength development, with the optimal curing conditions being high temperature and high humidity.

Conclusively, the results suggest that the addition of fly ash and silica fume can significantly enhance the strength development of LSG mixes,

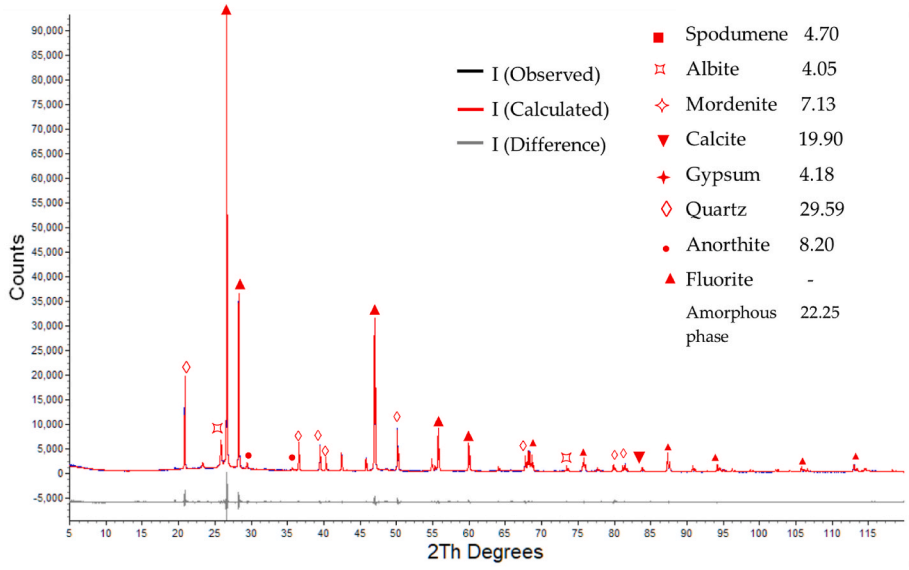

Fig. 16. Rietveld quantitative analysis of 60LS40SF$_{45}$.

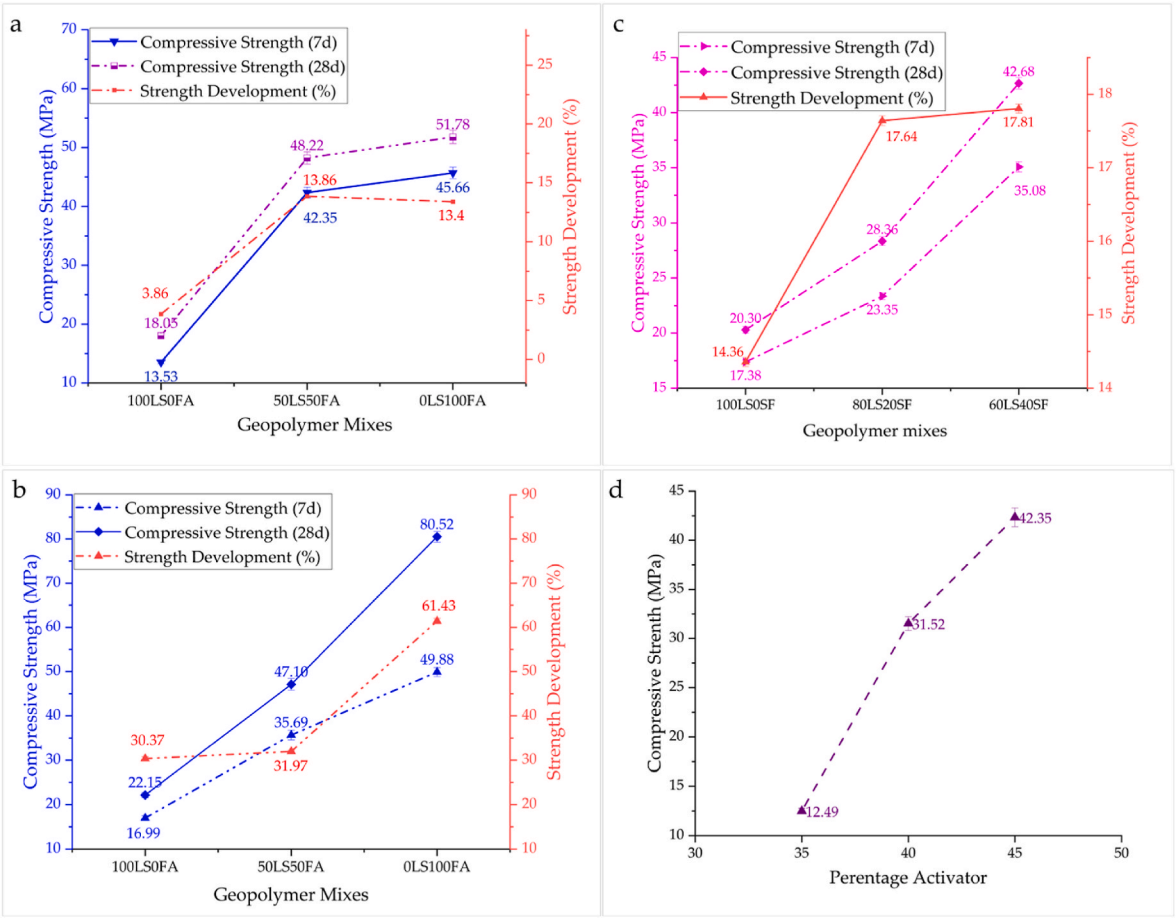

Fig. 17. Compressive strength and strength development of geopolymer composite at a) Fly ash incorporated LSG at 45% alkaline activator b) Fly ash incorporated LSG at 55% of alkaline activators c) Silica fume incorporated LSG at 45% of alkaline activators d) Compressive strength of lithium slag containing 50% fly ash at varying alkaline activator.

and a higher alkaline activator concentration can further improve the strength gain.

3.7. Relationship among mineralogy, microstructural morphology, rietveld refinement, and micromechanical properties

The synthesis of LSG involved the reaction of alkaline activators with precursors rich in aluminosilicate to create a Si-O-Al bond network in three dimensions. The mechanical properties of geopolymer are determined by the structural characteristics of elongated Si-O-Al bonds present in N-(C)-A-S-H gel. It is a scientific fact that an increase in activator content, characterized by a higher concentration of monovalent cations such as Na+, leads to the stabilization of the negatively charged AlO_4 tetrahedron. This results in the formation of a long-chained network structure of polysialate [15]. The quality of N-(C)-A-S-H is dependent upon the chemical, morphological, and crystallographic characteristics of the precursor while holding all other variables constant (such as temperature, activator content, curing conditions, and time). Lithium slag is an aluminosilicate source with a lower calcium content that bears a chemical resemblance to fly ash. The spodumene, anorthite, albite, amorphous phase, and some traces of other plagioclase feldspars constitute the aluminosilicates [18–20]. The amorphous phase of aluminosilicate exhibits higher reactivity compared to minerals possessing definite crystal structures and orientations [21].

The higher concentration of fly ash and silica fume and optimal alkaline activator have densified the microstructure and increased aluminosilicate dissolution. The elastic modulus (nano-indentation) and compressive strength were highest at 50% fly ash incorporation. Because fly ash contains more reactive silica in the form of aluminosilicate, quartz, and cristobalite. However, lithium slag is mostly spodumene, a stable mineral and a major source of aluminosilicates. Spodumene is less reactive to alkaline activators than fly ash, which mostly contains SiO_2 and Al_2O_3 with minor of Fe_2O_3, CaO, MgO, Na_2O, and K_2O. Fly ash's glassy, hollow, and porous nature makes it more susceptible to aluminosilicate dissolution in alkaline [93,94], while lithium slag's crystalline structure and solid micromorphology make it more alkaline-resistant. Spodumene in lithium slag forms insoluble hydroxides and carbonates in alkaline liquids [95,96]. Hence, spodumene requires greater alkaline activator concentrations, higher curing temperatures, and longer curing periods to attain comparable mechanical characteristics and microstructure to fly ash-based geopolymers. Thus, the geopolymer formed by fly ash has a higher initial strength but a lower potential for further strength development. Spodumene needs higher alkaline activator concentrations, higher curing temperatures, and longer curing time than fly ash-based geopolymers to match fly ash's mechanical properties and microstructure. Fly ash geopolymers have a higher initial strength but a lower strength development potential. However, lithium slag has less reactive silica in the amorphous phase and more sulphatic species, which dissolve and expand the microstructure [18]. Thus, anhydrite and sodium sulfate decrease initial strength but increase strength enhancement at higher alkaline activators, curing time, and temperature.

From mineral analysis, it is inferred that the presence of anorthite aluminosilicate gel exhibits better microstructural characteristics and notable contributions to the enhancement of LSG's strength due to its higher specific gravity (2.7) and hardness values (6–6.5 on the Mohs

hardness scale) in contrast to mordenite. Similarly, the hardness and elastic modulus of anorthite-based aluminosilicate gel determined from nanoindentation was higher than that of mordenite. The higher content and elastic modulus values of anorthite from PDF analysis at 45% alkaline activator are validated and are evidence of better microstructure development and higher compressive strength.

The coexistence of elevated levels of aluminosilicates and lithium is associated with favorable geochemical conditions. Nevertheless, increased quantities of sulfur in the form of anhydrite/gypsum may not be conducive to the development of zeolites and hydrates. The elevated levels of sulfur arise from the leaching process of spodumene ore for lithium extraction during the refining phase [20,22]. Higher concentrations of sulfate appear to induce cracking in N-(C)-A-S-H gel as reported by the published literature [18]. The production of lithium slag through the sulfation process results in a higher concentration of sulfate in the form of gypsum and anhydrite. The elevated sulfur concentration present in lithium slag could potentially be a contributing factor to the reduced strength development that is observed in the geopolymer blends that incorporate it. The reaction between sulfur and the aluminosilicate precursor in the geopolymer mixture can result in the formation of sulfoaluminate. This can have an adverse effect on the hydrolysis and condensation reactions that are responsible for the creation of a crosslinked network and subsequent increase in strength. The inclusion of sulphatic components in geopolymer does not result in the formation of ettringite as a sufficient CaO is required. However, the dissolution of sulfur forms an amorphous microstructure, and it becomes part of aluminosilicate gel. Similarly, Rattanasak et al. [97] incorporated sulfate admixture in fly ash geopolymer and reported the formation of sodium sulfate, which is similar to the formation of sodium sulfate and may have caused the flash setting in LSG in the authors' previous study [18]. In the published literature [18–20,22,98], the deleterious effect of sulfate is mitigated by the incorporation of sodium tetraborate and other precursors such as fly ash and silica fume. However, the effect of a higher concentration of alkaline activator could potentially suppress the formation of sulfur species in the aluminosilicate gel as evidenced by macro and micromechanical results, thus improving the mechanical properties of geopolymer. The increase in strength of heat-cured LSG at 70 °C for 24 h could be attributed to the ongoing reactions between the geopolymer and the curing environment. These reactions include the hydrolysis of the aluminosilicate precursor and the condensation of the resulting silanol groups (Si-OH) and aluminate tetrahedron (AlO^{4-}), leading to the formation of a crosslinked network and thus increased strength [99,100]. By losing moisture, silanol groups condense to create siloxane linkages (Si-O-Si). As a result, the aluminosilicate units in the geopolymer form a crosslinked network, increasing its strength. Temperature, hydrostatic pressure, pH, water content, the type of aluminosilicate precursor, and degree of carbonation all play important roles in hydrolysis and condensation reactions during geopolymerization [101].

The strength development mechanism is also significantly affected by carbonation in which the decalcification of aluminosilicate gel happens and pH lowers the susceptibility of durability attack, consequently resulting in the formation of calcite in the microstructure of the geopolymer paste matrix. There is overwhelming evidence for the formation of calcic polymorphs because of carbonation and various controlling carbonation-influencing parameters reported in the literature [80–82]. However, carbonation in LSG containing fly ash composites is recorded lower than that of silica fume incorporated mixes, also it decreases with the addition of silica fume thus densifying the microstructure.

Conclusively, the process of synthesizing geopolymer from lithium slag entails the interaction between alkaline activators and aluminosilicate-rich precursors, resulting in the formation of a three-dimensional Si-O-Al bond network. The mechanical properties of geopolymer are contingent upon the structural attributes of elongated Si-O-Al bonds that are found within the N-(C)-A-S-H gel. The analyses of microstructure and mineralogy indicated that the geopolymer derived from fly ash exhibited greater initial strength owing to its elevated reactive silica content in comparison to the geopolymer derived from lithium slag, which comprised spodumene (relatively less reactive than fly ash). The findings obtained through nanoindentation provided significant scientific knowledge for mineral identification based on their elastic modulus, as well as for assessing their strength and hardness. The higher modulus outcomes observed at 45% of alkaline activator were consistent with the results obtained from the mineral compositional analysis.

4. Conclusion

The study used micro-nano structural characterization techniques to understand the strength development mechanism of LSG which revealed that additive incorporation of fly ash and silica fume have synergic effects on the development of aluminosilicate gel. The strength development of LSG is primarily governed by the formation of C-(N)-A-S-H gel. Overall, the research highlights the potential use of lithium slag as a geopolymer precursor and studies the complex geochemistry of aluminosilicate gel formation during alkali activation. The salient conclusions of this research are as follows:

1. The mineral and morphological characterization of lithium slag indicates that the aluminosilicate exists in the form of spodumene, anorthite, and albite, whereas fly ash contains aluminosilicate in the form of albite, mullite, and anorthite. Although the aluminosilicate in fly ash is more crystalline than in lithium slag, however, fly ash offers higher dissolution of aluminosilicate than spodumene-based-mineral slag. This might be due to the stable and less-reactive response of spodumene in an alkaline environment as the spodumene forms insoluble compounds with hydroxide and carbonates while reacting with an alkaline solution. Therefore, spodumene requires a higher alkaline activator for the higher dissolution of aluminosilicates. Hence, the root cause of the lower strength of LSG without incorporation of fly ash and silica fume is attributed to the less reactive nature of spodumene and sulphatic components in lithium slag.
2. The higher dissolution of aluminosilicate in LSG containing fly ash at 45 and 55% of alkaline activator resulted in amorphous gel chained polytetrahedron consisting of covalently bonded oligomers of aluminosilicate alongside the formation of sodalite crystals that stiffens the skeleton of aluminosilicate gel owing to the alkali activation of fly ash cenospheres. Moreover, kaolinite was also formed after the geopolymerization of lithium slag particles.
3. The mineral analysis revealed that the C-(N)-A-S-H and N-(C)-A-S-H gel shares chemical similarities with anorthite and mordenite depicting the Si/Al ratios between 2.41 to 3.04 and 3.88 to 4.33, respectively. The C-(N)-A-S-H gel represented by anorthite offers higher elastic modulus and hardness properties as compared to N-(C)-A-S-H gel represented by mordenite on the mineral micrographs.
4. The microstructure was found to be weakened by the lower elastic moduli values of the mordenite phase at 55% concentrations of alkaline activators. However, the LSG containing 40% silica fume was found less affected by the formation of weaker microstructure.
5. The nano-indentation results depicted that among all tested mixes the highest quality microstructure was achieved for LSG containing fly ash at 45% alkaline activator marked by the higher percentage concentration (62%) and average elastic modulus (22.54 ± 1.20) of C-(N)-A-S-H gel in the geopolymer paste matrix, whereas at 55% alkaline activator of the same mix, the percentage concentration and elastic modulus values of C-(N)-A-S-H gel were 10.35 ± 1.42 and 34%, respectively.
6. The formation of amorphous aluminosilicate gel attributed to the strength of geopolymer is a widely accepted scientific fact, however, carbonation in geopolymer results in calcite polymorphs and causes the desiccation of aluminosilicate gel. The co-existence of calcite within aluminosilicate gel microstructure could have significantly

deteriorated in the LSG with no silica fume, however, reduction in carbonation occurred at 40% alkaline activator. The STEM, SAED, and Rietveld analysis identified and quantified the carbonation degree in terms of the formation of crystalline calcite as a carbonation product. SAED analysis of LSG containing 40% silica fume revealed the formation of amorphous aluminosilicate gel represented by halos, accompanied by few crystallites of calcite, thus evidencing carbonation. Moreover, carbonation almost doubled from 35% to 45% of alkali activator content in silica fume-incorporated LSG.

7. STEM presented deep insight into the formation of aluminosilicate gel in a typical HRTEM bright field image. The partially related lithium slag particle transitioned into aluminosilicate gel by a significant drop of Si/Al ratios from 5 to 3.48, whereas the Ca/Si ratio of aluminosilicate gel was 0.33.

CRediT author contribution statement

Usman Javed: Conceptualization, Data curation, Formal analysis, Investigation, Methodology, Visualization, Writing-original draft, Writing-review & editing. Faiz Uddin Ahmed Shaikh: Conceptualization, Funding acquisition, Project administration, Resources, Validation, Supervision, Writing-review & editing. Prabir Kumar Sarker: Supervision, Validation, Resources, Writing-review & editing.

Declaration of competing interest

The authors declare that they have no known competing financial interests or personal relationships that could have appeared to influence the work reported in this paper.

Data availability

Data will be made available on request.

Acknowledgment

The authors acknowledge to Australian Research Council (ARC), Australia for providing financial support in this research in the form of Discovery Project grant DP200102784.

The authors also acknowledge the use of the state-of-the-art Tescan Integrated Mineral Analyzer (TIMA), Scanning Electron Microscope (Tescan VEGA), Transmission Electron Microscope, and X-ray Diffractometer (D8 Discover) at John De Laeter Research Centre, Curtin University, Australia.

References

[1] J. Mills, P. Mondal, N. Wagner, Structure-property relationships and state behavior of alkali-activated aluminosilicate gels, Cement Concr. Res. 151 (2022).
[2] M.I.M. Alzeer, H. Nguyen, T. Fabritius, H. Sreenivasan, V.V. Telkki, A.M. Kantola, C. Cheeseman, M. Illikainen, P. Kinnunen, On the hydration of synthetic aluminosilicate glass as a sole cement precursor, Cement Concr. Res. 159 (2022).
[3] Y.R. Wang, Y.B. Cao, Z.H. Zhang, P. Zhang, Y.W. Ma, A.G. Wang, H. Wang, Intrinsic sulfuric acid resistance of C-(N)-A-S-H and N-A-S-H gels produced by alkali-activation of synthetic calcium aluminosilicate precursors, Cement Concr. Res. 165 (2023).
[4] A. Kusbiantoro, M.F. Nuruddin, N. Shafiq, S.A. Qazi, The effect of microwave incinerated rice husk ash on the compressive and bond strength of fly ash based geopolymer concrete, Construct. Build. Mater. 36 (2012) 695–703.
[5] G.Z. Zhang, Y. Li, J. Yang, Q.J. Ding, D.S. Sun, Insight into the strengthening mechanism of the Al-induced cross-linked calcium aluminosilicate hydrate gel: a molecular dynamics study, Front Mater 7 (2021).
[6] P. Perez-Cortes, J.I. Escalante-Garcia, Gel composition and molecular structure of alkali-activated metakaolin-limestone cements, Cement Concr. Res. 137 (2020).
[7] J.Q. Li, W.X. Zhang, P.J.M. Monteiro, Preferred orientation of calcium aluminosilicate hydrate compacts: implications for creep and indentation, Cement Concr. Res. 143 (2021).
[8] M.A.T. Marple, B. Koroglu, K. Morrison, J. Crowhurst, A. Balachandra, P. Soroushian, H.E. Mason, Accelerated carbonation and structural transformation of blast furnace slag by mechanochemical alkali-activation, Cement Concr. Res. 156 (2022).
[9] A. Fernandez-Jimenez, A. Palomo, M. Criado, Microstructure development of alkali-activated fly ash cement: a descriptive model, Cement Concr. Res. 35 (6) (2005) 1204–1209.
[10] V. Glukhovsky, Ancient, Modern and Future Concretes, Proceedings of the First International Conference on Alkaline Cements and Concretes, Kiev, Ukraine, 1994, pp. 1–8.
[11] H. Xu, J. Van Deventer, The geopolymerisation of alumino-silicate minerals, Int. J. Miner. Process. 59 (3) (2000) 247–266.
[12] P. Duxson, S.W. Mallicoat, G.C. Lukey, W.M. Kriven, J.S.J. van Deventer, The effect of alkali and Si/Al ratio on the development of mechanical properties of metakaolin-based geopolymers, Colloid. Surface. 292 (1) (2007) 8–20.
[13] C.J. Shi, A.F. Jimenez, A. Palomo, New cements for the 21st century: the pursuit of an alternative to Portland cement, Cement Concr. Res. 41 (7) (2011) 750–763.
[14] A. Fernandez-Jimenez, A. Palomo, I. Sobrados, J. Sanz, The role played by the reactive alumina content in the alkaline activation of fly ashes, Microporous Mesoporous Mater. 91 (1–3) (2006) 111–119.
[15] J. Davidovits, Geopolymer, Green Chemistry and Sustainable Development Solutions: Proceedings of the World Congress Geopolymer, Geopolymer Institute2005, 2005.
[16] X. Chen, P. Mondal, Effects of NaOH amount on condensation mechanism to form aluminosilicate, case study of geopolymer gel synthesized via sol-gel method, J. Sol. Gel Sci. Technol. 96 (3) (2020) 589–603.
[17] W.P. Zhu, X. Chen, L.J. Struble, E.H. Yang, Quantitative characterization of aluminosilicate gels in alkali-activated incineration bottom ash through sequential chemical extractions and deconvoluted nuclear magnetic resonance spectra, Cement Concr. Compos. 99 (2019) 175–180.
[18] U. Javed, F.U.A. Shaikh, P.K. Sarker, Microstructural investigation of lithium slag geopolymer pastes containing silica fume and fly ash as additive chemical modifiers, Cement Concr. Compos. 134 (2022).
[19] U. Javed, F.U.A. Shaikh, P.K. Sarker, Microstructural investigation of thermo-mechanically processed lithium slag for geopolymer precursor using various characterization techniques, Construct. Build. Mater. 342 (2022).
[20] J.X. Wang, L. Han, Z. Liu, D.M. Wang, Setting controlling of lithium slag-based geopolymer by activator and sodium tetraborate as a retarder and its effects on mortar properties, Cement Concr. Compos. 110 (2020).
[21] R.P. Williams, A. van Riessen, Determination of the reactive component of fly ashes for geopolymer production using XRF and XRD, Fuel 89 (12) (2010) 3683–3692.
[22] Z. Liu, J.X. Wang, Q.K. Jiang, G.D. Cheng, L. Li, Y.X. Kang, D.M. Wang, A green route to sustainable alkali-activated materials by heat and chemical activation of lithium slag, J. Clean. Prod. 225 (2019) 1184–1193.
[23] H.-K. Kim, H.-Y. Ha, J.-H. Bae, M.K. Cho, J. Kim, J. Han, J.-Y. Suh, G.-H. Kim, T.-H. Lee, J.H. Jang, Nanoscale light element identification using machine learning aided STEM-EDS, Sci. Rep. 10 (1) (2020) 1–12.
[24] A. C618, Standard Specification for Coal Fly Ash and Raw or Calcined Natural Pozzolan for Use in Concrete, C 618, 2022.
[25] S.Q. Luo, M. Liu, L. Yang, J.D. Chang, Effects of drying techniques on the crystal structure and morphology of ettringite, Construct. Build. Mater. 195 (2019) 305–311.
[26] J. Zhang, G.W. Scherer, Comparison of methods for arresting hydration of cement, Cement Concr. Res. 41 (10) (2011) 1024–1036.
[27] R. Kleeberg, T. Monecke, S. Hillier, Preferred orientation of mineral grains in sample mounts for quantitative XRD measurements: how random are powder samples? Clay Clay Miner. 56 (4) (2008) 404–415.
[28] B.D. Stemper, D. Board, N. Yoganandan, C.E. Wolfla, Biomechanical properties of human thoracic spine disc segments, J Craniovertebral Ju 1 (1) (2010) 18–22.
[29] A. Mehmood, N.M. Mubarak, M. Khalid, R. Walvekar, E.C. Abdullah, M.T. H. Siddiqui, H.A. Baloch, S. Nizamuddin, S. Mazari, Graphene based nanomaterials for strain sensor application-a review, J. Environ. Chem. Eng. 8 (3) (2020).
[30] A. Technologies, Agilent Nano Indenter G200 (2009).
[31] R. Böklen, in: H. Westbrook, H. Conrad (Eds.), The Science of Hardness Testing and its Applications, ASM, Metals Park, OH, 1973, p. 109.
[32] C.L. Hu, Microstructure and mechanical properties of fly ash blended cement pastes, Construct. Build. Mater. 73 (2014) 618–625.
[33] W.C. Oliver, G.M. Pharr, An improved technique for determining hardness and elastic-modulus using load and displacement sensing indentation experiments, J. Mater. Res. 7 (6) (1992) 1564–1583.
[34] R.J. Thomas, S. Peethamparan, Alkali-activated concrete: engineering properties and stress-strain behavior, Construct. Build. Mater. 93 (2015) 49–56.
[35] M. Sofi, J.S.J. van Deventer, P.A. Mendis, G.C. Lukey, Engineering properties of inorganic polymer concretes (IPCs), Cement Concr. Res. 37 (2) (2007) 251–257.
[36] M. Noorpour, A. Tarighat, Effects of Si/Al ratio on structure, modulus of elasticity, and density in N-A-S-H geopolymer: a molecular dynamics simulation based on novel macromolecular model, J. Mol. Model. 27 (11) (2021).
[37] Y. Zhang, J.L. Zhang, J.Y. Jiang, D.S. Hou, J.R. Zhang, The effect of water molecules on the structure, dynamics, and mechanical properties of sodium aluminosilicate hydrate (NASH) gel: a molecular dynamics study, Construct. Build. Mater. 193 (2018) 491–500.
[38] B. Kim, S. Lee, C.M. Chon, S. Cho, Setting behavior and phase evolution on heat treatment of metakaolin-based geopolymers containing calcium hydroxide, Materials 15 (1) (2022).
[39] Z.H. Zhang, H. Wang, J.L. Provis, F. Bullen, A. Reid, Y.C. Zhu, Quantitative kinetic and structural analysis of geopolymers. Part 1. The activation of metakaolin with sodium hydroxide, Thermochim. Acta 539 (2012) 23–33.

[40] C.A. Rios, C.D. Williams, O.M. Castellanos, Crystallization of low silica Na-A and Na-X zeolites from transformation of kaolin and obsidian by alkaline fusion, Ing Compet 14 (2) (2012) 125–137.

[41] K.M. Klima, K. Schollbach, H.J.H. Brouwers, Q.L. Yu, Enhancing the thermal performance of Class F fly ash-based geopolymer by sodalite, Construct. Build. Mater. 314 (2022).

[42] Z.B. Chen, X.L. Wan, Y.F. Qian, J.L. Qiao, J.X. Jia, L. Mo, M.L. Gao, H. Cui, Y. Liu, F.F. Min, The effect on the compressive strength of fly ash based geopolymer concrete with the generation of hydroxy sodalite, Construct. Build. Mater. 309 (2021).

[43] W. Franus, M. Wdowin, M. Franus, Synthesis and characterization of zeolites prepared from industrial fly ash, Environ. Monit. Assess. 186 (9) (2014) 5721–5729.

[44] A. Fernández-Jiménez, F. Zibouche, N. Boudissa, I. García-Lodeiro, M.T. Abadlia, A. Palomo, "Metakaolin-Slag-Clinker blends." the role of Na+ or K+ as alkaline activators of theses ternary blends, J. Am. Ceram. Soc. 96 (6) (2013) 1991–1998.

[45] J.L. Provis, J.S.J. van Deventer, Geopolymerisation kinetics. 2. Reaction kinetic modelling, Chem. Eng. Sci. 62 (9) (2007) 2318–2329.

[46] J. Hovelmann, A. Putnis, T. Geisler, B.C. Schmidt, U. Golla-Schindler, The replacement of plagioclase feldspars by albite: observations from hydrothermal experiments, Contrib. Mineral. Petrol. 159 (1) (2010) 43–59.

[47] A. Hassan, M. Arif, M. Shariq, Influence of microstructure of geopolymer concrete on its mechanical properties—a review, Advances in Sustainable Construction Materials and Geotechnical Engineering: Select Proceedings of TRACE (2020) 119–129, 2018.

[48] M.F. Doerner, W.D. Nix, A method for interpreting the data from depth-sensing indentation instruments, J. Mater. Res. 1 (4) (1986) 601–609.

[49] R. Rodriguez, I. Gutierrez, Correlation between nanoindentation and tensile properties Influence of the indentation size effect, Mat Sci Eng a-Struct 361 (1–2) (2003) 377–384.

[50] M.A.G. Maneiro, J. Rodriguez, Pile-up effect on nanoindentation tests with spherical-conical tips, Scripta Mater. 52 (7) (2005) 593–598.

[51] D.J. Shuman, A.L.M. Costa, M.S. Andrade, Calculating the elastic modulus from nanoindentation and microindentation reload curves, Mater. Char. 58 (4) (2007) 380–389.

[52] N.X. Randall, M. Vandamme, F.J. Ulm, Nanoindentation analysis as a two-dimensional tool for mapping the mechanical properties of complex surfaces, J. Mater. Res. 24 (3) (2009) 679–690.

[53] G. Constantinides, K.S.R. Chandran, F.J. Ulm, K.J. Van Vliet, Grid indentation analysis of composite microstructure and mechanics: principles and validation, Mat Sci Eng a-Struct 430 (1–2) (2006) 189–202.

[54] M. Nedeljkovic, B. Savija, Y.B. Zuo, M. Lukovic, G. Ye, Effect of natural carbonation on the pore structure and elastic modulus of the alkali-activated fly ash and slag pastes, Construct. Build. Mater. 161 (2018) 687–704.

[55] J. Nemecek, V. Smilauer, L. Kopecky, J. Nemeckova, Nanoindentation of alkali-activated fly ash, Transport. Res. Rec. 2141 (2010) 36–40.

[56] Webmineral, Mordenite Mineral Data, 2021. http://webmineral.com/data/Mordenite.shtml#.ZFEwHM5BytU. (Accessed 2 May 2023).

[57] Webminerals, Anorthite Mineral Data, 2023. https://webmineral.com/data/Anorthite.shtml.

[58] Z.Y. Luo, W.G. Li, Y.X. Gan, X.Z. He, A. Castel, D.C. Sheng, Nanoindentation on micromechanical properties and microstructure of geopolymer with nano-SiO2 and nano-TiO2, Cement Concr. Compos. 117 (2021).

[59] Z.Y. Luo, W.G. Li, K.J. Wang, S.P. Shah, D.C. Sheng, Nano/micromechanical characterisation and image analysis on the properties and heterogeneity of ITZs in geopolymer concrete, Cement Concr. Res. 152 (2022).

[60] D. Tranchida, S. Piccarolo, On the use of the nanoindentation unloading curve to measure the Young's modulus of polymers on a nanometer scale, Macromol. Rapid Commun. 26 (22) (2005) 1800–1804.

[61] W.Y. Yan, C.L. Pun, G.P. Simon, Conditions of applying Oliver-Pharr method to the nanoindentation of particles in composites, Compos. Sci. Technol. 72 (10) (2012) 1147–1152.

[62] T. Akatsu, S. Numata, T. Demura, Y. Shinoda, F. Wakai, Representative indentation elastic modulus evaluated by unloading of nanoindentation made with a point sharp indenter, Mech. Mater. 83 (2015) 66–71.

[63] R.C. Chang, F.Y. Chen, P.H. Yang, Dynamic mechanical properties of photo resist thin films, J. Mech. Sci. Technol. 21 (10) (2007) 1739–1744.

[64] V. Bewick, L. Cheek, J. Ball, Statistics review 9: one-way analysis of variance, Crit. Care 8 (2004) 1–7.

[65] S. Parsons, Encyclopedia of measurement and statistics, 3 vol, Ref. User Serv. Q. 46 (4) (2007), 87-87.

[66] R. Ylmen, U. Jaglid, Carbonation of portland cement studied by diffuse reflection fourier transform infrared spectroscopy, Int J Concr Struct M 7 (2) (2013) 119–125.

[67] J.F. Young, R.L. Berger, J. Breese, Accelerated curing of compacted calcium silicate mortars on exposure to Co2, J. Am. Ceram. Soc. 57 (9) (1974) 394–397.

[68] D. Shi, J.Y. Ye, W.S. Zhang, W.G. Shen, Properties, mineralogy and microstructure evolution of 4-year calcium silicate slag-based alkali-activated materials, Cement Concr. Compos. 136 (2023).

[69] S.A. Bernal, R.M. de Gutierrez, J.L. Provis, V. Rose, Effect of silicate modulus and metakaolin incorporation on the carbonation of alkali silicate-activated slags, Cement Concr. Res. 40 (6) (2010) 898–907.

[70] J. Zhang, C.J. Shi, Z.H. Zhang, Effect of Na2O concentration and water/binder ratio on carbonation of alkali-activated slag/fly ash cements, Construct. Build. Mater. 269 (2021).

[71] J. Zhang, C.J. Shi, Z.H. Zhang, Carbonation induced phase evolution in alkali-activated slag/fly ash cements: the effect of silicate modulus of activators, Construct. Build. Mater. 223 (2019) 566–582.

[72] K. Behfarnia, M. Rostami, An assessment on parameters affecting the carbonation of alkali-activated slag concrete, J. Clean. Prod. 157 (2017) 1–9.

[73] Y. Lv, J. Qiao, W. Han, B. Pan, X. Jin, H. Peng, Modification effect of Ca (OH) 2 on the carbonation resistance of fly ash-metakaolin-based geopolymer, Materials 16 (6) (2023) 2305.

[74] N. Werling, F. Dehn, F. Krause, A. Steudel, R. Schuhmann, K. Emmerich, Solubility of precursors and carbonation of waterglass-free geopolymers, Clay Clay Miner. 68 (5) (2020) 524–531.

[75] J.J. Chen, J.J. Thomas, H.M. Jennings, Decalcification shrinkage of cement paste, Cement Concr. Res. 36 (5) (2006) 801–809.

[76] M. Liesegang, R. Milke, C. Kranz, G. Neusser, Silica nanoparticle aggregation in calcite replacement reactions, Sci. Rep. 7 (2017).

[77] D. Baizar, H. Ledbetter, Accurate modeling of size and strain broadening in the Rietveld refinement: the "double-Voigt" approach, Adv. X Ray Anal. 38 (1994) 397–404.

[78] F. Puertas, M. Palacios, T. Vazquez, Carbonation process of alkali-activated slag mortars, J. Mater. Sci. 41 (10) (2006) 3071–3082.

[79] N. Li, N. Farzadnia, C.J. Shi, Microstructural changes in alkali-activated slag mortars induced by accelerated carbonation, Cement Concr. Res. 100 (2017) 214–226.

[80] M. Castellote, C. Andrade, X. Turrillas, J. Campo, G.J. Cuello, Accelerated carbonation of cement pastes in situ monitored by neutron diffraction, Cement Concr. Res. 38 (12) (2008) 1365–1373.

[81] H.W. Song, S.J. Kwon, Permeability characteristics of carbonated concrete considering capillary pore structure, Cement Concr. Res. 37 (6) (2007) 909–915.

[82] T. Yang, B. Keller, E. Magyari, K. Hametner, D. Gunther, Direct observation of the carbonation process on the surface of calcium hydroxide crystals in hardened cement paste using an Atomic Force Microscope, J. Mater. Sci. 38 (9) (2003) 1909–1916.

[83] Z.J. Li, S.F. Liu, Influence of slag as additive on compressive strength of fly ash-based geopolymer, J. Mater. Civ. Eng. 19 (6) (2007) 470–474.

[84] T. Koumoto, Production of high compressive strength geopolymers considering fly ash or slag chemical composition, J. Mater. Civ. Eng. 31 (8) (2019).

[85] N.P. Tran, T.N. Nguyen, T.D. Ngo, P.K. Le, T.A. Le, Strategic progress in foam stabilisation towards high-performance foam concrete for building sustainability: a state-of-the-art review, J. Clean. Prod. 375 (2022).

[86] A.R.K. Gollakota, V. Volli, C.M. Shu, Progressive utilisation prospects of coal fly ash: a review, Sci. Total Environ. 672 (2019) 951–989.

[87] S. Dadsetan, H. Siad, M. Lachemi, O. Mahmoodi, M. Sahmaran, Sodium glass liquid from glass waste as a user-friendly hardener in structural geopolymer systems, Cement Concr. Compos. 130 (2022).

[88] M. Zhang, H.Y. Xu, A.L.P. Zeze, X.F. Liu, M.J. Tao, Coating performance, durability and anti-corrosion mechanism of organic modified geopolymer composite for marine concrete protection, Cement Concr. Compos. 129 (2022).

[89] J.H.M. Visser, Fundamentals of alkali-silica gel formation and swelling: condensation under influence of dissolved salts, Cement Concr. Res. 105 (2018) 18–30.

[90] M.T. Ghafoor, Q.S. Khan, A.U. Qazi, M.N. Sheikh, M.N.S. Hadi, Influence of alkaline activators on the mechanical properties of fly ash based geopolymer concrete cured at ambient temperature, Construct. Build. Mater. 273 (2021).

[91] G.S. Ryu, Y.B. Lee, K.T. Koh, Y.S. Chung, The mechanical properties of fly ash-based geopolymer concrete with alkaline activators, Construct. Build. Mater. 47 (2013) 409–418.

[92] A.B. Malkawi, M.F. Nuruddin, A. Fauzi, H. Almattarneh, B.S. Mohammed, Effects of alkaline solution on properties of the HCFA geopolymer mortars, Procedia Eng. 148 (2016) 710–717.

[93] J. van Jaarsveld, J. Van Deventer, Effect of the alkali metal activator on the properties of fly ash-based geopolymers, Ind. Eng. Chem. Res. 38 (10) (1999) 3932–3941.

[94] H. Xu, J. Van Deventer, The geopolymerisation of natural alumino-silicates, Proc. 2nd Internat. Conf. Geopolymere (1999) 43–63.

[95] A. Karrech, M. Dong, M. Elchalakani, M.A. Shahin, Sustainable geopolymer using lithium concentrate residues, Construct. Build. Mater. 228 (2019).

[96] V. Maneta, D.R. Baker, W. Minarik, Evidence for lithium-aluminosilicate supersaturation of pegmatite-forming melts, Contrib. Mineral. Petrol. 170 (1) (2015).

[97] U. Rattanasak, K. Pankhet, P. Chindaprasirt, Effect of chemical admixtures on properties of high-calcium fly ash geopolymer, Int J Min Met Mater 18 (3) (2011) 364–369.

[98] Q. Luo, Y.S. Wang, S.X. Hong, F. Xing, B.Q. Dong, Properties and microstructure of lithium-slag-based geopolymer by one-part mixing method, Construct. Build. Mater. 273 (2021).

[99] R. Dupuis, S.H. Hahn, A.C.T. van Duin, R.J.M. Pellenq, A. Poulesquen, Condensation and growth of amorphous aluminosilicate nanoparticles via an aggregation process, Phys. Chem. Chem. Phys. 24 (16) (2022) 9229–9235.

[100] L. Weng, K. Sagoe-Crentsil, Dissolution processes, hydrolysis and condensation reactions during geopolymer synthesis: Part I - low Si/Al ratio systems, J. Mater. Sci. 42 (9) (2007) 2997–3006.

[101] X.K. Shi, D. Graiver, R. Narayan, Hydrolysis and condensation of hydrophilic alkoxysilanes under acidic conditions, Silicon-Neth 4 (2) (2012) 109–119.